

1. INTRODUCTION

In a crystal lattice, atoms are arranged in a very regular manner and form a spatial periodic potential. As a consequence of this periodic potential, bands of allowed and forbidden energies are formed, for example in semiconductor materials those bands include the valence band, and the conduction band which are separated by the band gap. The theory related to the motion of electrons through a one-dimensional periodic potential was first described by the Kronig-Penney model. Due to the new growth techniques, it has become possible to construct artificial one dimensional (1D) lattice structures by growing different layers of materials on top of each other. In general, the periodic change of a potential, i.e. a series of potential wells separated by potential barriers, is referred to as a Multiple Quantum Well.

In practice, a quantum well can be constructed by means of a thin layer of one narrower-bandgap semiconductor, surrounded by two wider-bandgap semiconductor layers, with the energy "minimum" for electrons and holes occurring in the narrower-bandgap semiconductor. The narrower bandgap layer yields a "potential well" for both electrons and holes, both of which will find lower energy in that layer; hence the term "well" in "quantum well". When the layer is made sufficiently thin, quantum confinement effects become apparent. For example, the layers with thickness of typically about 10 nm, the quantum effects are very obvious even at room temperature in typical semiconductors. The essence of the quantum effects can be understood qualitatively, through the simple "particle in a box" or "infinite quantum well" model.

The material growth techniques such as Molecular Beam Epitaxy (MBE) and Metal-Organic Chemical Vapor Deposition (MOCVD), created the practical possibility of controllably making more precise structures so thin that they could exhibit quantum mechanical confinement effects. This led to basic proposals in the early 1970's, first of superlattice structures that might show interesting resonant tunneling effects for possible negative resistance devices, and secondly for quantum well structures that might show improved semiconductor laser operation. Though quantum-confined structures remain interesting for electronic devices, it is in optoelectronics that the quantum confinement in thin layers has proved particularly fruitful for practical and useful devices.

Quantum wells and related structures have a broad range of uses for applications from telecommunications to optical storage. The use of quantum wells in some existing devices, such as high-speed optical modulators, high-performance laser diodes, intersubband photodetectors, and quantum-cascade lasers, they form possible devices without analogs in bulk materials. They also can be used simply to adjust the effective bandgap of materials without changing the underlying material compositions, an option

that is useful especially when the material growth is constrained by lattice matching requirements. Because quantum-confined structures can be made relatively easily, when one is growing heterostructures using modern growth techniques, they have become a routine part of many advanced optoelectronic devices, and they can be combined with mirrors, waveguides, transistors, and other optical and electronic devices.

As the semiconductor industry is nearing the limits of performance improvements for the current technologies dominated by silicon, there is a constant search for novel, non-traditional materials whose properties can be controlled by electrical fields. Most notable examples of such materials developed recently are organic conductors [1], oxides near a superconducting of magnetic phase transition [2] and carbon nanotubes [3-4]. Carbon nanotubes are widely considered as a possible base material for future electronics. However, growth and/or selection of nanotubes with a particular chirality (depending on the chirality, electronic properties of nanotubes vary strongly) remain a distant goal with many groups working in this direction. On the other hand, planar graphene offers a viable alternative. In comparison with nanotubes, graphene films have some advantages. The obvious advantages are their uniform, reproducible properties, low contact resistances, absence of the Schottky barrier and their large size.

The renowned properties of the graphene-based materials clearly indicate that planar graphene is a remarkable material, for example, it is stable at room temperature up to 3500°C. It is extremely flexible similar to carbon nanotubes, but at the same time as hard to tear apart as diamond. Electronic properties of planar graphene are extraordinary: so that, room temperature in plane mobility (μ) in graphite can reach 15,000 and, possibly up to 100,000 cm^2/Vs , while at liquid-helium temperatures, graphite routinely exhibits a carrier mobility above $10^6 \text{ cm}^2/\text{Vs}$, [5]. This means, the charge carriers in graphene layers can move without scattering at relatively large (submicron) distances even at room temperature. This would make graphene films very tempting from the point of view of microelectronics applications. Despite being effectively only a single atomic layer thick with respect to their electronic properties, the films exhibit remarkably high quality so that high mobility two-dimensional electron and hole gases can be formed by applying external electric field. Based on the switching between 2D electron and 2D hole gases, the observed properties of graphene devices prove that they can be used as metallic field-effect transistors (FET). Indeed, a factor of 30 in the on-off current ratio is considered to be sufficient for logic circuits.

The aim of this thesis is to obtain the energy levels for i.e., the band structure in a multi-quantum well system and a finite size superlattice. The influence of those energy levels on the boundary condition and the number of quantum wells in the structure is investigated. For example, I will investigate when a miniband structure is revealed as function of the number of quantum wells. The effect of an electric field (uniform and nonuniform) on the energy levels is investigated. This leads to the so-called Stark effect with the appearance of Wannier-Stark states. I will apply these techniques to already a new system formed of graphene layers and a field effect transistor based on such graphene layers.

2. QUANTUM WELLS AND SUPERLATTICES

2.1 Semiconductor Heterostructures

If more than one semiconductor material is used in a device, this device is sometimes called a heterostructure device. A heterojunction is formed when two different materials are joined together at a junction. It is now possible to make such heterojunctions extremely abrupt through the modern materials growth processes; in fact, heterojunction interfacial thickness may be fabricated on a dimensional scale approaching only one atomic monolayer. The simplest heterostructure is a structure that consists of one heterojunction of two different semiconductor materials. There is a rich selection of various materials (semiconductors, metals, and insulators) that leads to high-quality interfaces and permits the fabrication of different heterostructures that manifest desired electron characteristics as functions of applied potentials. The most well-known and applicable example is the Si/SiO₂ heterojunction with a very small density of defects at the interface. The following pairs of semiconductor III-V compounds have great importance in technological applications and in studies of the properties of heterostructures such as GaAs/AlGaAs, GaInAs/InP, GaInAs/AlInAs, GaSb/AlSb, GaN/AlN, InN/GaN, ...,etc. Another class of actively studied and applied heterostructures are based on the II-VI compounds such as CdZnSe/ZnSe, ZnSTeSe/ZnSSe,....etc.

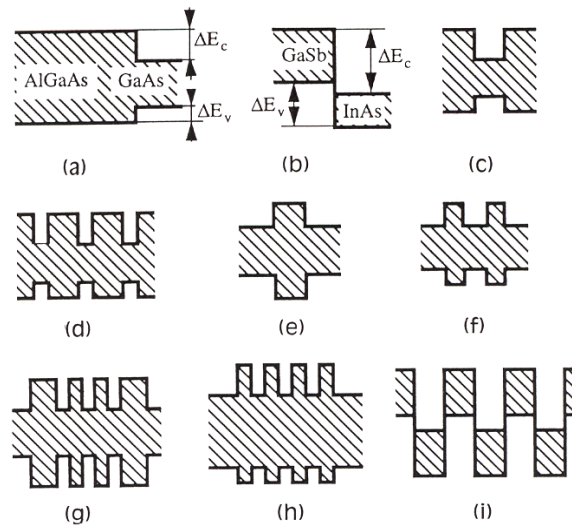


Figure 2.1. Energy band diagram for different semiconductor heterostructures; (h) and (i) represent type-I and type-II superlattices respectively, [from V. Mitin, 1999].

One of the major goals of the fabrication of heterostructures is the controllable modification of the energy bands of carriers. Energy-band diagrams for several semiconductor heterostructures are shown in Fig. (2.1). This figure illustrates the following: (a), (b) two types of single-junction heterostructures; (c), (e) different double-junction heterostructures; (f) a quaternary-junction heterostructure; and (d), (g), (h), (i) several multiple-junction structures. It is important that the energy positions of conduction and valence bands on different sides of heterojunctions differ by an amount of the order of a few hundreds of meV or more. These energies exceed by a considerable amount the thermal energy of carriers under typical operational conditions. This is why carriers can be confined easily inside the electrically active regions of a heterostructure bounded by potential barriers. These electrically active regions are frequently referred to as potential wells. In two special limiting cases, potential wells may be classified straightforwardly as classical and quantum wells. The width of the classical well is large compared with the de Broglie wavelength of an electron or a hole in the well. In the other limit, for a quantum well, Fig. (2.1.c), the width is comparable with or smaller than the de Broglie wavelength. For this case, the classical treatment of carrier motion breaks down and quantum behavior is manifested clearly.

Actually, besides discontinuities of energy bands, there are other factors that control the profile of the potential and other properties of propagating electrons. In real devices these factors include a space-dependent composition of compounds, a dependence on spatial-coordinate of doping, an electrostatic potential, different effective masses in layers composing a heterostructure, possible mechanical strain of layers,... etc.

2.2 Growth of Heterostructures

Heterostructures must have interfaces of particularly high quality in order to perform well. The atomic structures (lattice parameters) of the two materials must match closely one to another [see Fig. (2.2)], and the interface must not be contaminated with impurities or suffer from other defects. In addition the layers may be thin, so one must be able to change the composition of successive layers very rapidly, preferably from one monolayer to another. Older methods of growing semiconductors such as Liquid-Phase Epitaxy (LPE) met some of these criteria and have been used for coarser structures such as double-heterostructure lasers, but more specialized processes are generally needed. The most widespread methods are Molecular-Beam Epitaxy (MBE) and Metal-Organic Chemical Vapor Deposition (MOCVD).

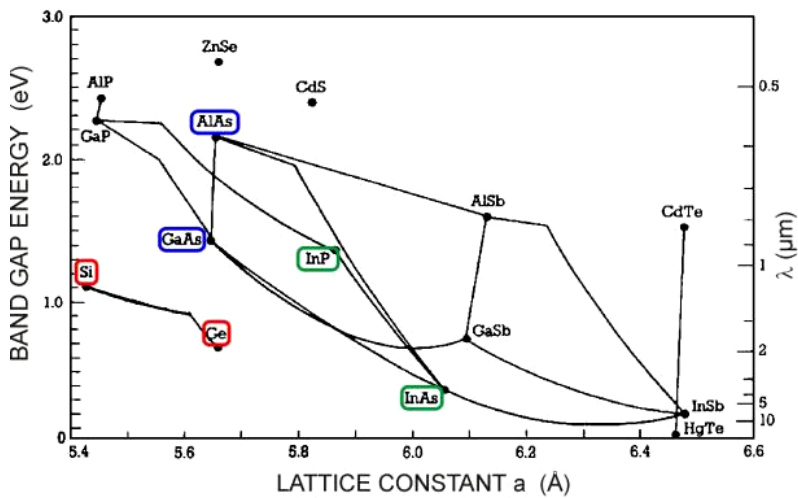


Figure 2.2. Lattice constant versus energy gap at room temperature for various III-V semiconductors, [from Tien, 1985].

MBE is capable of controlling deposition of submonolayer coverage on a substrate and has become one of the most important epitaxial techniques. Almost every semiconductor has been grown by this technique. MBE is a high vacuum technique ($\sim 10^{-11}$ torr, vacuum when fully pumped down) in which crucibles containing a variety of elemental charges are placed in the growth chamber Fig. (2.3). The elements contained in the crucibles make up the components of the crystal to be grown as well as the dopants that may be used. When a crucible is heated, atoms or molecules of the charge are evaporated and these travel in straight lines to impinge on a heated substrate.

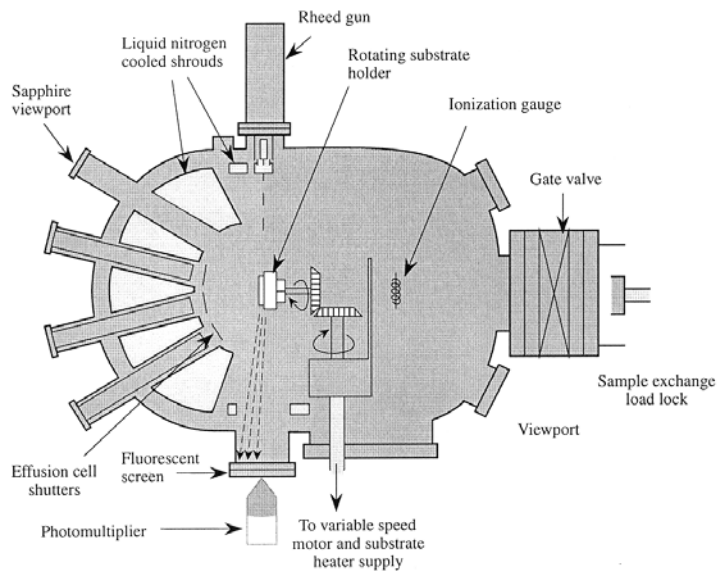


Figure 2.3. A schematic of a typical MBE growth system, [from J. Singh, 2003].

The growth rate in MBE is about 1 monolayer ($\sim 3 \text{ \AA}$) per second and this slow rate coupled with shutters placed in front of the crucibles allow one to switch the composition of the growing crystal with monolayer control. Since no chemical reactions occur in MBE, the growth is the simplest of all epitaxial techniques and is quite controllable. However, since the growth involves high vacuum, leaks can be a major problem. The growth chamber walls are usually cooled by liquid N_2 to ensure high vacuum and to prevent atoms/molecules to come off from the chamber walls.

The low background pressure in MBE allows one to use electron beams to monitor the growing crystal. The reflection high energy electron diffraction (RHEED) technique relies on electron diffraction to monitor both the quality of the growing substrate and the quasi layer by layer growth mode.

2.3 Band Engineering with Semiconductor Heterostructures

The whole point of growing heterostructures is the opportunity that they offer the possibility to manipulate the behavior of electrons and holes through *band engineering*. It is essential to look in more detail at the conduction (E_c) and valence (E_v) bands themselves. Consider a heterojunction between two materials A and B, with $E_g^A < E_g^B$. The simplest theory yields Anderson's rule, which is based on the electron affinity χ of the materials, the energy required to take an electron from the bottom of the conduction band E_c to the vacuum level where it can escape from the crystal. The electron affinity is nearly independent of the position of the Fermi level, unlike the work function, which is measured from the Fermi level and therefore depends strongly on doping. Anderson's rule states that the vacuum levels of the two materials of a heterojunction should be lined up, as in Fig. (2.4). This shows immediately that $\Delta E_c = E_c^B - E_c^A = \chi^A - \chi^B$. For example, GaAs has $\chi = 4.07 \text{ eV}$ and $\text{Al}_{0.3}\text{Ga}_{0.7}\text{As}$ has $\chi = 3.74 \text{ eV}$, predicting $\Delta E_c = 0.33 \text{ eV}$. The band gap changes by $\Delta E_g = 0.37 \text{ eV}$, so $\Delta E_v = 0.04 \text{ eV}$. The fraction of the band gap that has gone into the conduction band $Q = \Delta E_c / \Delta E_g = 0.85$ according to this model [6].

Although it is easy to measure the difference in band gap, it is much more difficult to resolve the discontinuity in the individual bands. The value $Q = 0.85$ just given was long used for $\text{Al}_x\text{Ga}_{1-x}\text{As}$, but the smaller value $Q = 0.62$ is now firmly established for $x < 0.45$ where the gap remains direct. Many experiments, such as optical absorption in rectangular quantum wells, prove to be only weakly sensitive to Q . Other shapes of quantum wells, such as parabolic potentials, give a better resolution [6].

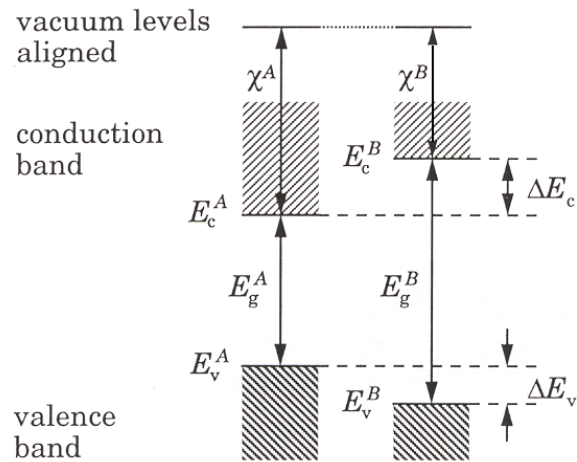


Figure 2.4. Anderson's rule for the alignment of the band at a heterojunction between materials A and B, [from J.H. Davies, 1998].

In the case of GaAs/AlGaAs, the narrower band gap is enclosed within the wider band gap, as shown in Fig. (2.4). Thus a sandwich with GaAs as the filling between two layers of AlGaAs traps both electrons and holes. This is called type-I or *straddling alignment* like in Fig. (2.1.a). There are two other possibilities for two different closely lattice-matched materials. InAs and GaSb show type II or *staggered alignment* like in Fig. (2.1.b), where the bands favor electrons in InAs but holes in GaSb, [Sakaki et al., 1977]. Thus a sandwich results in a potential well for one species but a barrier for the other. The other possibility is that the two band gaps do not overlap at all, giving type-III or *broken-gap alignment*. In this case the conduction band of one material overlaps the valence band of the others (like the usual band structure of semimetals, e.g., graphite).

2.4 Superlattice Band Structure

Superlattices are one-dimensional quantum confined structures that were first proposed theoretically in 1970's by L. Esaki and R. Tsu, who investigated the properties of one-dimensional periodic potential and negative differential conductivity in semiconductors. And subsequently, superlattices were developed experimentally by the well-known material growth techniques, with dimensional control close to interatomic spacing. By the improvement of semiconductor based superlattice structures, unusual optical and electrical properties have been observed and detailed band structure engineering has become possible.

In principle, superlattices consist of two different semiconductor materials interleaved in thin layers by depositing them in alternation. And hence, they can be depicted as a periodic alternation of the band gap energies of those two semiconductors. The alternation leads the band edges to exhibit a periodic variation with the position along the growth direction and form a series of barriers perpendicular to the motion of the charge carriers. There are two methods by which the potential inside the superlattice could be varied. One is alternating the alloy composition between the layers (compositional superlattices) and the other is to change the impurity density during the crystal growth (doped superlattices). The alternation from one type of semiconductor with a particular band gap to another type of semiconductor with a different band gap and then back to the original semiconductor forms the potential profile of the superlattices. The relevant quantities here are thus the change in band gap energies and the conduction/valence band alignment of each semiconductor. Going from one type of semiconductor to another gives an abrupt change in band energy that effects the propagation of the electrons in the lattice. Relevant to the possibility of actually forming a superlattice is essentially the crystal structure of the inherent materials. The lattice parameters of each material should match closely so that the transition from one material to another would be as smooth as possible [see Fig. (2.2)].

The Transmission Electron Microscope (TEM) image of a typical GaAs/AlGaAs superlattice is shown in Fig. (2.5) (the image is recorded at UA/EMAT for the course of TEM in Advanced Master in Nanophysics Program, academic year 2003-2004). And the corresponding potential profile is presented in Fig. (2.6) in which the wells and the barriers have simple rectangular forms. The theory of real superlattices is not simple, because the real wells and the barriers have complex profiles. In addition, the effective masses can be different in the wells and the barriers. Moreover, as the thicknesses of wells and barriers are reduced to a few atomic monolayers, the commonly used effective-mass approximation would not be applicable.

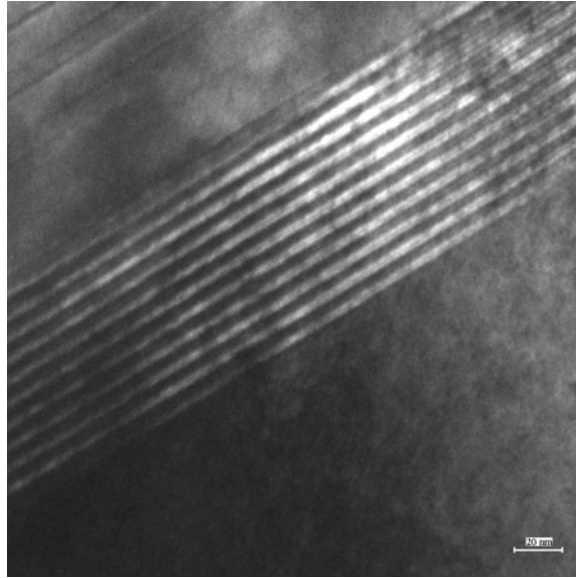


Figure 2.5. Transmission Electron Microscope (TEM) image of a typical (GaAs/AlGaAs) superlattice.

To understand the basic behavior of superlattice structures, one should use the experience accumulated in the problem of periodic structures in crystals and then illustrate the major properties of the structure presented in Fig. (2.6); this structure can be described by the well known Kronig-Penney model, which is a principal model for one-dimensional crystals in solid-state physics. The only essential difference is that one needs to modify the Kronig-Penney model by using the effective mass m^* instead of the free-electron mass m_0 , with ($m^* < m_0$).

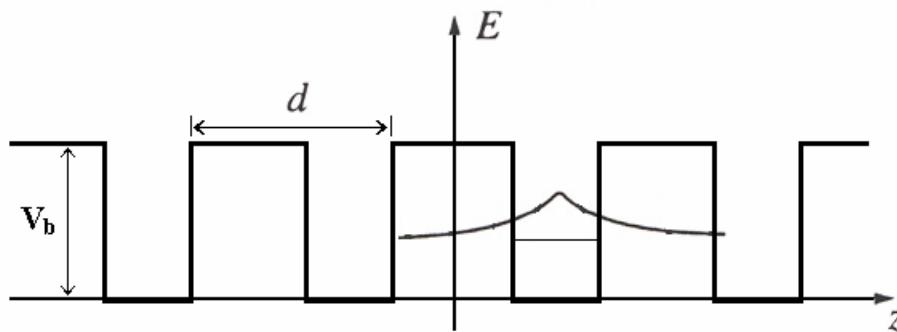


Figure 2.6. Schematic presentation of the potential profile of a superlattice with period d . The energy level and wavefunction are shown for a single well.

According to the Kronig-Penney model, any energy level of the single well E_i splits into a series of N levels, where N is the number of the wells in the superlattice, as depicted in Fig. (2.7.a). The physical reason of this splitting may be viewed as being caused by electron tunneling among the wells. For a N -well system with high and thick barriers between the wells, in the first approximation the energy levels coincide with their single-well positions, but they are N -fold degenerate. Tunneling between the wells breaks the degeneracy and results in a splitting into N levels with the wavefunctions common for all the wells. This implies that in any of these states one can find electrons inside any well. It is worth noting that a width of the energy region occupied by these levels is independent of the number of wells N , if N is large. This energy region is the so-called energy band and it depends only on the tunneling characteristics of the system.

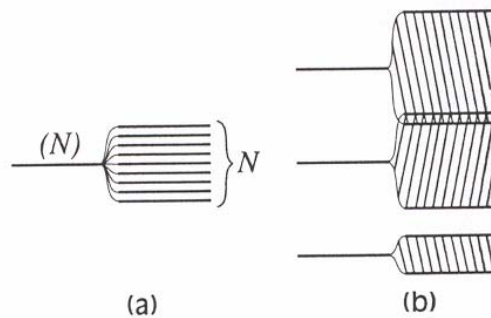


Figure 2.7. Schematic presentation of formation of superlattice minibands [from V. Mitin, 1999].

Generally energy bands appear for any system that exhibits this tunneling-induced coupling and does not require periodicity. Indeed, disordered condensed materials are also characterized by energy bands. However, the periodicity brings about additional nontrivial behavior of the system, for an electron in an ideal crystal. This periodicity leads to the condition that the physical characteristics of the system do not change when the electron is shifted exactly by one period or an integer number of periods. Applying this requirement to the wave function, one gets a direct analog of the Bloch theorem,

$$\psi(z + nd) = C_n \psi(z) = \exp(iqnd) \psi(z) \quad (2.1)$$

where $d = (l_w + l_b)$ is the period of the superlattice, l_w and l_b are the thickness of the wells and the barriers respectively. Eq. (2.1) introduces a new parameter in the wavefunction, namely, the one-dimensional wave (Bloch wave) vector q . Wavefunctions with different values of q obey different transformations in accordance with Eq. (2.1). The wave functions corresponding to different states of the same energy band are characterized by different values of q . Thus q is a new quantum number of the system. In addition, one can introduce a hypothetical length of the superlattice Nd and exploit the cyclic boundary conditions,

$$\psi(z + Nd) = \psi(z) \quad (2.2)$$

This yields the relationship $\exp(iqNd) = 1$ and $q = [(2\pi/Nd)p]$ where $p = 1, 2, \dots, N$. The latter relationship implies that the total number of quantum states arising as a result of the coupling of the N identical, uncoupled single-well levels is the same as the number of the wells in the superlattice (note that spin is not considered). The spacing between neighboring values of q is equal to $2\pi/Nd$. It is customary to introduce the following interval for q ,

$$\left\{ -\frac{\pi}{d}, \frac{\pi}{d} \right\}$$

which is the first Brillouin zone for the electrons in a superlattice.

As just discussed, the energy band originates from the N isolated levels of the N single quantum wells as the well separation is decreased and the tunneling coupling among the wells is thereby increased. It is clear that each energy level of an isolated single quantum well evolves into an energy band containing N levels when N such isolated quantum wells are coupled through tunneling effects to form a superlattice; see Fig. (2.7.a). Because of the periodicity, each band is characterized by a Bloch wave vector q , so that for the i^{th} level one obtains the band $E_i(q)$. Since the tunneling probability increases with increasing level index i , the width of the bands also increases with i . The narrowest band is the lowest one. Frequently the higher bands in superlattices overlap. This situation is sketched in Fig. (2.7.b).

Important features of superlattices are the bandgaps and the new manmade dispersion curves $E_i(q)$ that characterize the energy states of the superlattice. The bandgaps, of course, define the energy intervals in which propagating states, the Bloch waves, do not exist. In these intervals electrons cannot propagate in the superlattice.

The dispersion relation $E_i(q)$ for the model presented in Fig. (2.6) can be calculated in the so-called tight-binding approximation when the Bloch wavefunctions are constructed from the wave functions of the single-well problem with the specified potential. Thus the wavefunction for the superlattice band i that originates from the energy level i can be written as,

$$\psi_{i,q}(z) = \frac{1}{\sqrt{N}} \sum_n \exp(iqnd) \psi_i(z - nd). \quad (2.3)$$

When the wavefunction of Eq. (2.3) is substituted into the Schrödinger equation with the superlattice potential $V(z) = \sum_n V(z - nd)$ and the coupling with the nearest-neighbor wells are taken into account, it follows that the energy of the i^{th} subband is,

$$E_i(q) = E_i + s_i + 2t_i \cos(qd). \quad (2.4)$$

where s_i and t_i are the shift and the transverse integrals respectively, which can be defined in the following form,

$$s_i \equiv - \int_{-\infty}^{\infty} dz \psi_i^*(z - d/2) V(z + d/2) \psi_i(z - d/2) \quad (2.4.a)$$

$$t_i \equiv - \int_{-\infty}^{\infty} dz \psi_i^*(z - d/2) V(z - d/2) \psi_i(z + d/2) \quad (2.4.b)$$

The relation for $E_i(q)$ is shown schematically in Fig. (2.8) (note that t_i is negative). The dispersion curve reveals the downshift in energies, in the present case, two neighboring wells are taken into account. Instead of the previous splitting into two levels with energies separated by $2|t_i|$ there is an entire continuum-energy band of width $\Delta E_i = 4|t_i|$. One can see that the width does not depend on the number of wells in the superlattice. The last term of Eq. (2.4) gives the dispersion relation for the i^{th} energy band. These superlattice bands are frequently referred to as minibands. The bandwidths of minibands are finite and determined by the transfer integral and depend strongly on the superlattice parameters, like the barrier thickness.

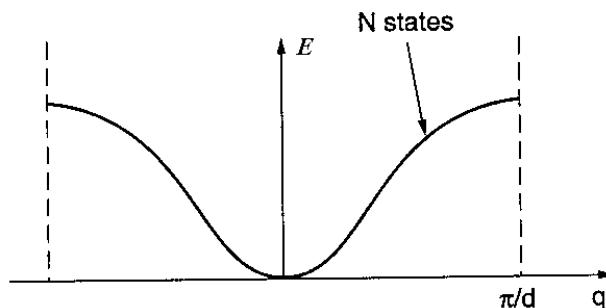


Figure 2.8. The dispersion curve concerning to the first miniband of a superlattice, [from V. Mitin, 1999].

So far, only the transverse propagation (i.e., the propagation along the axis of the superlattice) of the electron was studied. The total electron energy including the energy associated with the in-plane propagation is,

$$E_i(\vec{k}, q) = E_i + s_i + \frac{\hbar^2 k_{\parallel}^2}{2m_{\parallel}^*} - 2|t_i| \cos(qd) \quad (2.5)$$

where k_{\parallel} is the two-dimensional wave vector in the (x, y) plane and m_{\parallel}^* is the parallel effective mass in the same plane. This formula demonstrates how dramatically the electron spectrum is modified and controlled by an artificial lattice.

Near the bottom and the top of the minibands it is possible to simplify further the energy spectrum of Eq. (2.5). Using the series expansion of $\cos(qd)$ leads to the following approximation around the point $q = 0$,

$$E_i(\vec{k}, q) = E_i + s_i - 2|t_i| + \frac{\hbar^2 k_{\parallel}^2}{2m_{\parallel}^*} + \frac{\hbar^2 q^2}{2M_i} \quad (2.6)$$

where M_i is the transverse effective mass in z -direction and is determined by the transfer integral, in accordance with the tunneling character of the transverse propagation. Eq. (2.6) reveals that the electron propagation is extremely anisotropic. The anisotropy is controlled by the thickness of the layers as well as the height of the barriers. Another interesting aspect of the dispersion curve of Eq. (2.5) is the existence of a portion of the dispersion curve with a negative effective mass where the second derivative of E_i with respect to q changes its sign at $q = \pi/2d$. Near the top of the miniband, the effective mass associated with transverse propagation is equal to $-M_i$. The existence of the negative effective mass means that the electron is propagating in the direction opposite to the applied force.

In general, the mass of an electron in a superlattice is roughly one order of magnitude larger than typical effective masses of bulk crystals, while widths of the minibands are relatively small. This is why low temperatures are preferable for applications of miniband effects.

2.5 Size Dependence of Superlattice Band Structure

Because of the small energy differences between the minibands, absorption between the minibands can be used to detect the infrared radiation (ir), for instance, for certain infrared applications it is desirable to have only two minibands with a small energy minigap. This could be achieved by varying the lattice parameters, which are width and the height of the potential barriers as well as the width of the wells [7]. In practice, the properties (width, position...etc.) of the minibands and corresponding minigaps are strongly influenced by the size of the barrier and/or well material, i.e., the bands become narrower and the gaps become wider as the barriers between wells become thicker. To obtain small transition energies in the superlattice this requires small barrier heights and large well widths. Furthermore, a precise control over both the barrier height and the well width is essential [7].

For the simple Kronig-Penney model that is sketched in Fig. (2.6), the $\cos(qd)$ term in the energy dispersion relation can be expanded in the following form;

$$\cos(qd) = \cos q(l_w + l_b), \quad (2.7)$$

$$\cos q(l_w + l_b) = \cos k_w l_w \cos k_b l_b - \frac{k_w^2 + k_b^2}{2k_w k_b} \sin k_w l_w \sin k_b l_b, \quad (2.8)$$

where $l_w = (d - l_b)$ is the width of the well between barriers, k_w the wavenumber in the wells, and k_b that in the barriers. This expression is for $E > V_b$ with all waves propagating; the usual substitution $k_b \rightarrow i\kappa_b$ for $E < V_b$ gives,

$$\cos q(l_w + l_b) = \cos k_w d \cosh \kappa_b l_b - \frac{k_w^2 - \kappa_b^2}{2k_w \kappa_b} \sin k_w d \sinh \kappa_b l_b, \quad (2.9)$$

A useful theoretical simplification of the rectangular barrier is the δ -function barrier. We keep $V_b l_b = S$ constant while letting $V_b \rightarrow \infty$ and $l_b \rightarrow 0$. Then Eq. (2.9) reduces to,

$$\cos(qd) = \cos k_w d + \left(\frac{m^* d S}{\hbar^2} \right) \frac{\sin k_w d}{k_w d}. \quad (2.10)$$

For $|\cos(qd)| \leq 1$, the Bloch wavenumber q is real for propagating states.

By using the dispersion relation one can predict the size dependence of the transverse and parallel effective masses, which give rise to the energy spectrum of the miniband. As discussed previously, the energy spectrum is defined by the Eq. (2.5). In that expression, it was shown that there is a clear relation between the energy spectrum and the transverse and the parallel effective masses. Any variation in transverse and parallel masses would directly affect the energy spectrum of the minibands. The transverse and parallel effective masses can be expressed in terms of effective masses in each component material (m_w and m_b) as well as the width of both well and barrier layers (l_w and l_b).

In semiconductor case, now we assume that E_w^c and E_b^c are the conduction band-edges of well and barrier layers respectively which is shown in Fig. (2.9). Then the band-offset, which is nothing else than the barrier height (V_b), can be defined as $V_{off} = E_b^c - E_w^c$ for $E_b^c > E_w^c$.

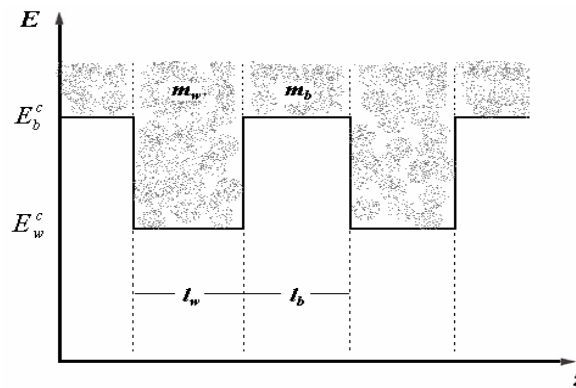


Figure 2.9. Profile of conduction band edges in a superlattice.

By introducing the effective masses, width of constituent materials and band-offset into the dispersion relation and solving the resultant equation perturbatively, we get an explicit definition for the transverse effective mass and parallel effective mass in terms of the layer thicknesses and band-offset [8],

$$M_i = \frac{m_w l_w + m_b l_b}{l_w + l_b} \left(1 + \frac{l_w^2 l_b^2 (m_b - m_w)}{3\hbar^2 (l_w + l_b)^2} V_{off} \right) \quad (2.11)$$

$$\frac{1}{m_{\parallel}^*} = \frac{l_w}{m_w (l_w + l_b)} + \frac{l_b}{m_b (l_w + l_b)} - \frac{l_w^2 l_b^2 (m_w l_w + m_b l_b)}{3\hbar^2 (l_w + l_b)^3} \left(\frac{1}{m_b} - \frac{1}{m_w} \right) V_{off}. \quad (2.12)$$

with a heavier effective mass in the barrier material than in the well material. The resultant transverse effective mass will be heavier, and the parallel effective mass lighter. These explicit formulae allow one to see directly how the miniband parameters depend on the layer widths, the effective masses in the components and the height of the barrier (band-offset, V_{off}).

2.6 Effect of Electrical Field on the Superlattice Band

In superlattices one can present the influence of an electrical field on the miniband energy spectrum by taking into account the electron motion in the miniband structure [9]. The finite bandwidth opens the possibility of observing and applying novel effects that takes place in any periodic system when an electric field is applied. If there is no electron scattering, the electron gains energy in an electric field until it reaches the top of the band where the Bloch wave q reaches the boundary of the Brillouin zone. Then the electron reflects back and continues its propagation in the opposite direction, decelerating until it reaches the bottom of the band. Then it accelerates again.

This process repeats over and over. Thus an electron in a miniband of finite bandwidth oscillates in real space and in momentum space. These oscillations are known as Bloch oscillations. Electron scattering destroys these oscillations. The oscillations of charged electrons lead to the emission of electromagnetic radiation. In the quantum picture discussed previously, the energy miniband is composed of a set of discrete-energy levels. In the presence of an electric field, band-bending lifts the energy degeneracy that produces the superlattice minibands and the energy spectrum of a superlattice with large N becomes an energy ladder of N discrete levels. Such an energy spectrum is known as a Stark ladder.

Transitions between the levels lead to emission or absorption of electromagnetic radiation (such as infrared and microwave radiation). These processes have been known for many

decades, but in bulk crystals the bandwidths are so large that electrons cannot reach the top of the band in the ballistic regime, i.e., without scattering. Because the bandwidth can be controlled and ballistic propagation along the superlattice axis can occur, superlattices provide a unique possibility for observing these effects.

2.6.1 Bloch Oscillations

Let us consider the motion of an electron along the superlattice axis z . For an electron in some miniband n with energy $E_n(k)$, the semiclassical equations of motion in an electric field are,

$$\frac{dp_z}{dt} \equiv \hbar \frac{dk_z}{dt} = -eF. \quad (2.13)$$

$$v_z(k_z) = \frac{1}{\hbar} \frac{dE_n(k_z)}{dk_z}. \quad (2.14)$$

The solution of Eq. (2.13) for a constant electric field is,

$$k_z(t) = k_z(0) - eFt / \hbar. \quad (2.15)$$

Therefore the wave vector k_z increases linearly with time. However, it is known that for a superlattice, one can consider the wave vector only inside the reduced Brillouin zone $\{-k_{Br}, k_{Br}\}$. Once the electron reaches the boundary of this zone k_{Br} , it appears at the point $(-k_{Br})$ of the reduced Brillouin zone representation.

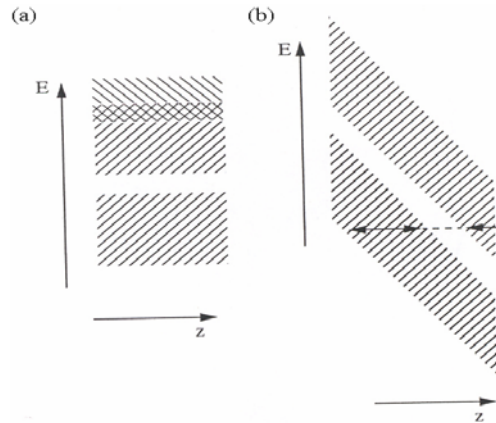


Figure 2.10. Schematic representation of energy spectra for a superlattice.
 (a) several bands in the absence of an electric field

(b) the same as case (a), biased by an electric field [from V. Mitin, 1999].

The electron velocity $v_z(k_z)$ given by Eq. (2.14) in the interval $(-k_{Br}, 0)$ has one opposite sign to the velocity in the interval $(0, -k_{Br})$. This is the reason why this phenomenon is closely reminiscent of a classical reflection from a rigid boundary and is referred to as Bragg reflection. Then the electron continues its motion according to Eqs. (2.13) and (2.14). Under these conditions, the electron motion is periodic, i.e., the velocity oscillates, as may be obtained from Eqs. (2.13) and (2.14), and the energy is restricted by the miniband width. Because the width of the Brillouin zone is equal to $2\pi/d$, where d is the spatial period of the superlattice, one can find the time period T_B and the frequency f_B of the electron oscillations,

$$T_B = \frac{1}{f_B} = \frac{2\pi}{\omega_B} = \frac{2\pi}{d} \frac{\hbar}{eF}. \quad (2.16)$$

The electron motion in real space is also characterized by the same periodic oscillations and these oscillations are commonly referred to as *Bloch oscillations*. Fig. (2.8) illustrates the dispersion relation $E(k)$ of the lowest miniband of a superlattice in the absence of an electric field. Other energy minibands are shown schematically in Fig. (2.10.a). In an electric field, the semiclassical energy of the electron changes as,

$$E^{(tot)}(z, k) = E(k) - eFz. \quad (2.17)$$

This spatial dependence is presented in Fig. (2.10.b). From this figure, one can see that an electron with fixed total energy $E^{(tot)}$ oscillates in the space region between two turning points (limited by the Brillouin zone) corresponding to the bottom and the top of the tilted miniband. This implies that the electrons are localized in some spatial region. If the electric field increases, the slope of the minibands increases and the degree of the electron localization increases as well.

According to the semiclassical relationship of Eq. (2.17), the size of the localization region δz decreases by a factor Δ_{mb}/eF , where Δ_{mb} is the miniband width.

2.6.2 Quantum Confined Wannier-Stark Effect

We have seen that the electric field in a superlattice leads to electron localization; therefore, in a high electric field, the semiclassical considerations of the Bloch oscillation section must be corrected from a quantum-mechanical point of view. In the so-called one-band approximation, the Schrödinger equation for the motion of the electrons along the superlattice axis takes the form,

$$\left[\hat{E} \left(-i \frac{d}{dz} \right) - eFz \right] \psi(z) = E \psi(z) \quad (2.18)$$

where the first term is the kinetic-energy operator of this motion. In this operator, the wave vector k_z in the miniband energy dispersion $\hat{E}(k_z)$ is replaced by the operator $[-i(d/dz)]$. An example of the dispersion relation $E(k_z)$ for a superlattice has been given by Eq. (2.4) and it has a more complicated form than the quadratic form $(-\hbar^2 k_z^2 / 2m^*)$ that we are accustomed to. The second term is the potential energy of the electrons in an electric field. An analysis of Eq. (2.18) shows that the electron-energy spectrum is no longer a continuum. Indeed, it splits into a series of levels with an equidistant energy separation proportional to the electric field. This splitting is known as Stark splitting. If the electron wave function $\psi(z)$ is a solution of Eq. (2.18) with some energy, say E_0 , and then the function $\psi(z - nd)$ is also a solution of the same equation with energy,

$$E = E_0 + neFd \quad (2.19)$$

where n is an integer. The set of these solutions constitutes the Wannier-Stark ladder of energy levels. The ladder is infinite, and the energy-level separation is $E = eFd$.

The quantity E may be expressed in terms of the Bloch oscillation frequency of Eq. (2.16),

$$\Delta E = \hbar\omega_B. \quad (2.20)$$

As it is discussed, in the absence of an electric field, the electron wavefunction $\psi(z)$ is extended throughout the superlattice. If the field is nonzero, the wavefunction is localized in a region with a size that decreases as the field increases, as shown in Fig. (2.11.a) and Fig. (2.11.b).

The electron is confined in one of the quantum wells for the high-field limit, as illustrated by Fig. (2.11.b). Hence the Wannier-Stark energy ladder corresponds to energy states, which can be approximately attributed to different quantum wells. A comparison of the previous analysis and that of this subsection leads us to the conclusion that the Bloch oscillations are the counterpart in the time domain of the stationary-state Wannier-Stark ladder in the energy domain.

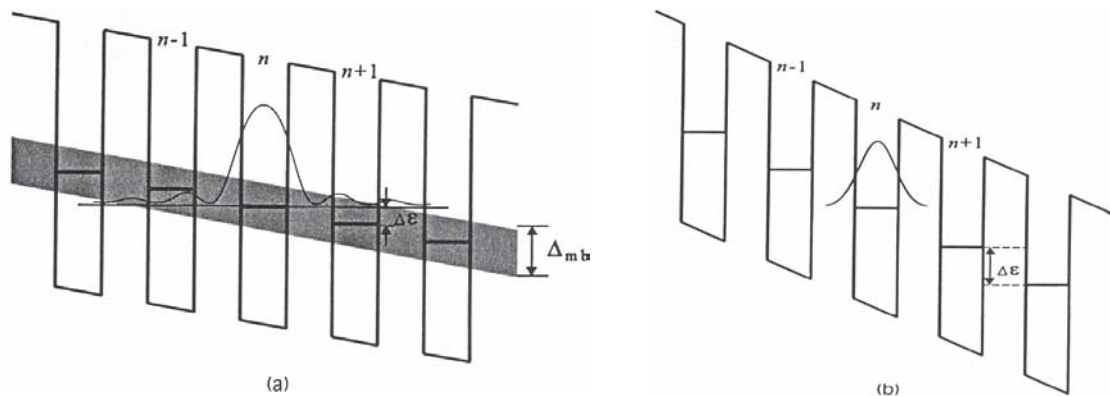


Figure 2.11. Schematic of wavefunction in a biased superlattice: (a) wavefunction from

the n^{th} well extends over several periods of the superlattice when ($E < \Delta_{\text{mb}}$)
(b) wavefunction is localized in the n^{th} well when ($E > \Delta_{\text{mb}}$), [from V. Mitin, 1999].

Both of these superlattice effects have been beyond the possibility of experimental demonstration for a long time. But recently, as superlattice structures have become sufficiently better - constant period, small defect densities, high transverse mobility,... etc. - the Wannier-Stark ladder has been observed. Experiments have been done mainly by use of optical methods. Measurements of photocurrent and light absorption, electro reflectance spectroscopy, and other methods have been applied to study the superlattices. In our previous discussions, we have considered superlattices based on layered structures. Another approach, with considerable potential for becoming a reality, is being developed by use of lateral systems. For example, such a lateral Bloch oscillator can consist of a double periodic array of metal dot gates embedded in the metal-oxide-semiconductor field-effect transistor (MOSFET). These gates induce a two-dimensional superlattice potential in the inversion layer. The electron concentration and the energy levels in minibands can be controlled by both the dot gates and the principal gate of the structure.

3. THE NUMERICAL METHOD

3.1 Finite Difference Technique

Approximate solution techniques like finite element, finite difference and finite volume are among the most often used methods to solve the Schrödinger equation. These methods are used to go from continuous models to discrete models. By this process, differential equations are replaced by linear or non-linear systems of algebraic equations whose solutions approximate the solutions of the original equations. While steps involved in these methods are well understood, the complexity in deriving such discretisation schemes can be very high. Symbolic computation can help to deal with the complexity as well as aid in the derivation of new solution schemes.

The finite difference technique is a method for solving partial differential equations (PDEs). For example a PDE will involve a function $u(x)$ defined for all x in a domain with respect to some given boundary condition. The purpose of the method is to determine an approximation to the function $u(x)$.

The method requires the domain to be replaced by a grid. At each grid point each term in the partial differential is replaced by a difference formula, which may include the values of u at that and neighboring grid points. By substituting the difference formulae into the PDE, a difference equation is obtained.

3.2 Numerical Solution of the Schrödinger Equation

Perhaps, solving the finite barrier problem analytically is the easiest way to obtain the energy states, however, it isn't so versatile. To solve more complicated band structures in one-dimensional time independent Schrödinger equation, we have chosen to use the finite difference technique. By using this technique, the Schrödinger eigenvalue problem can be transformed into a matrix eigenvalue problem.

The one-dimensional Schrödinger equation is given by,

$$-\frac{\hbar^2}{2m} \frac{d^2}{dx^2} \psi(x) + V(x)\psi(x) = E\psi(x), \quad (3.1)$$

with the potential $V(x)$ in which the particle mass m is moving in. In the finite difference technique, one replaces this second order differential equation with a set of coupled linear equations. One starts with discretising the domain in which one wants to calculate the

wavefunction $\psi(x)$, in N grid points, as shown in Fig. (3.1). The value of x in point n is given by $x_n = x_{\min} + (n-1)h$ with the step size $h = (x_{\max} - x_{\min})/(N-1)$. Now we want to calculate the value of the wavefunction in each grid point namely ψ_n for $n = 1, \dots, N$. The second derivative $d^2\psi(x)/dx^2$ in the point x_n can be approximated by the following finite difference approximation;

$$\left. \frac{d^2\psi(x)}{dx^2} \right|_{x_n} \approx \frac{\psi_{n+1} - 2\psi_n + \psi_{n-1}}{h^2}, \quad (3.2)$$

with this expression we can discretise the Schrödinger equation (3.1) as follows,

$$-\frac{\hbar^2}{2m} \frac{\psi_{n+1} - 2\psi_n + \psi_{n-1}}{h^2} + V(x_n)\psi_n = E\psi_n \quad (3.3)$$

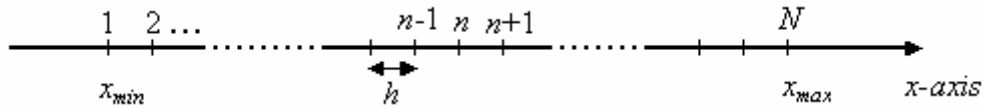


Figure 3.1. The grid points.

The set of Eqs. (3.3) is now equivalent to,

$$H\tilde{\psi} = E\tilde{\psi} \quad (3.4)$$

with a matrix H given by,

$$H = \frac{\hbar^2}{2m} \begin{pmatrix} 2 & -1 & 0 & 0 & \dots & 0 & 0 \\ -1 & 2 & -1 & 0 & \dots & 0 & 0 \\ 0 & -1 & 2 & -1 & \dots & 0 & 0 \\ & & \ddots & \ddots & \ddots & & \\ 0 & 0 & 0 & 0 & \dots & 2 & -1 \end{pmatrix} + \begin{pmatrix} V(x_1) & 0 & \dots & 0 \\ 0 & V(x_2) & \dots & 0 \\ & & \ddots & \\ 0 & 0 & \dots & V(x_N) \end{pmatrix} \quad (3.5)$$

Diagonalisation of this matrix will give the result, namely the eigenvalues which are the discrete energies, and the eigenvectors, which correspond to the eigenfunctions. The accuracy of the results depends on the number of chosen grid points, and of the chosen end points x_{\max} and x_{\min} . The end points must be chosen in such a way that the resulting eigenfunctions become zero at these boundaries.

4. MINIBAND FORMATION AND SURFACE STATES

4.1 Introduction

Modeling of the superlattice can be performed by solving the Schrödinger equation for a one-dimensional system that alternates in voltage (or potential) between two constant values. To solve the Schrödinger equation, we implemented the finite difference technique by using the Matlab programming language. By means of this program we solved the 1D Schrödinger equation for many different potentials in order to model the superlattice. The first problem is to find the solutions of the Schrödinger equation and compare the results with the analytical solution of the infinitely deep square well. This is a test of the program to verify if it is producing valid wavefunctions and valid energy values. Next the program will be extended to the case of a square well of finite depth. The solutions for this potential are also well known and again serve to verify the numerical program.

Next the program will be extended to a multiple potential well system. The periodic change in potential with distance is what is present in superlattices. We will investigate how does the band formation occur in the superlattices and how does it depend on the superlattice parameters.

At the end, the numerical program will be extended to the case when an electric field is applied to the superlattice. In this case, the potential increases with position, requiring the Schrödinger equation to be solved for a periodic potential with a ramp function between any two individual wells. The effect of such an electric field on the energy levels and wavefunctions will be investigated. Finally, the results obtained from the whole numerical calculations will be applied to a real system which is based on graphene layers.

4.2 Modeling of Infinitely Deep Quantum Well

In order to test the numerical program if it gives valid energy values with the corresponding wavefunctions, the finite difference technique is applied to solve the one-dimensional time-independent Schrödinger equation for infinitely deep quantum well. The Schrödinger equation for an infinitely deep quantum well with a potential height of $V(z) \rightarrow \infty$ at the boundaries is written as,

$$-\frac{\hbar^2}{2m} \frac{d^2\psi(z)}{dz^2} = E\psi(z), \quad (4.1)$$

and at the well boundaries $\psi(z) = 0$.

The solution of Eq. (4.1) gives the energy spectrum,

$$E_n = \frac{\hbar^2 \pi^2}{2mL^2} n^2 \quad \text{for } n = 1, 2, 3, \dots \quad (4.2)$$

where L is the width of the well, for $n = 1$, we obtain the ground state energy E_0 which will be the energy unit for all our further calculations,

$$E_0 = \frac{\hbar^2 \pi^2}{2mL^2} \quad (4.3)$$

For numerical calculations it is convenient to represent the variables in dimensionless units. This technique is helpful to implement the Schrödinger equation into a computer program. Thus, if the Schrödinger equation is divided by the energy unit E_0 ,

$$-\frac{1}{\pi^2} \frac{d^2}{dz^2} \psi(z) = \left(\frac{E}{E_0} \right) \psi(z) \quad (4.4)$$

The solution of the equation gives the energy spectrum [$E_n = E_0 n^2$], in the units of (E/E_0) and the corresponding wavefunctions $\psi(z)$ as function of the position of (z/L) .

So far, the necessary expressions for the numerical calculations of infinite well have been defined. By applying the Eq. (4.4) in our program, the first three energy levels and corresponding wavefunctions of the infinitely deep quantum well are calculated and sketched in Fig. (4.1).

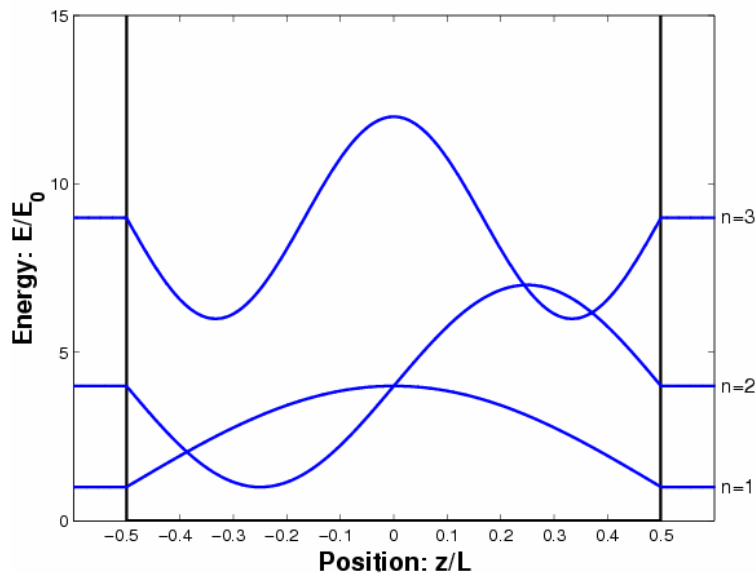


Figure 4.1. First three energy levels and corresponding wavefunctions, (which are shifted vertically by their corresponding energy) of an infinite quantum well.

According to the obtained result, the energies are well quantized and take part in discrete levels. The wavefunctions vanish on either side of the well. We checked that the numerical results are equal to the analytical expressions.

4.3 Modeling of Finite Height Quantum Well

In this section we performed our calculation for a finite depth quantum well in which the barrier height is taken to be a finite value. Thus, if we take E_0 as dimensionless unit and L (width of the well) as length unit, the Schrödinger equation can be written in dimensionless form as,

$$\left[-\frac{1}{\pi^2} \frac{d^2}{dz^2} + \frac{V(z)}{E_0} \right] \psi(z) = \left(\frac{E}{E_0} \right) \psi(z) \quad (4.5)$$

where $V(z) = V_b$ for $z/L \leq -0.5$ and $z/L \geq 0.5$ is the height of the barriers. We solved the differential equation numerically by discretising the position in a base with size sufficiently larger than the width of the quantum well. The first four energy levels and their corresponding wavefunctions are depicted in Fig. (4.2). In the calculation the height of the barriers is taken to be $V_b = 20E_0$, for either side of the well.

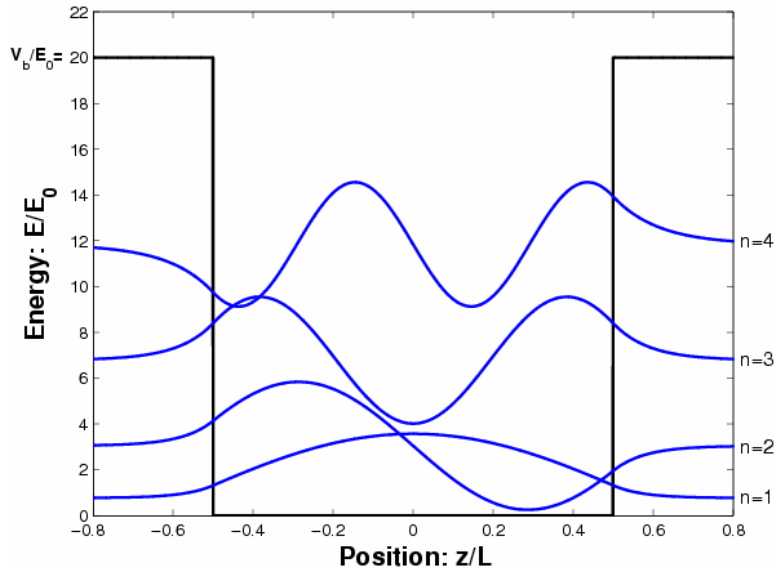


Figure 4.2. First four energy levels and corresponding wavefunctions of a finite quantum well. The wave functions are shifted by their corresponding energy.

Notice that, as the effective height of the barrier decreases, i.e., $V_b - E_n$, the wavefunction penetrates deeper into the barrier region. We found that changing the size of the well strongly influences the energy levels as well as the corresponding wave functions. For example, when the thickness of the well decreases, the levels start to shift-up in energy. This demonstrates that the specific properties of a quantum well can be tuned by its size parameters like the thickness and depth of the quantum well.

4.4 Coupling Between Symmetric Quantum Wells

In principle coupling effect between two symmetric and isolated wells can be observed roughly in three ways. One is to decrease the height of the barrier located in the middle of the wells. The second is to decrease the thickness of the same barrier by keeping its height to be constant. And the third way is raising the number of barriers in a particular region of the well.

First we inserted a potential barrier with height $V_b = 20E_0$ in the middle of an infinite quantum well ($L = 2w + b$). The thickness of the barriers (b) is taken to be equal to the thickness of the separated wells (w), which gives the ratio $w/b = 1$. By this way a symmetric double well system is formed. Increasing the ratio from $w/b = 0.1$ to $w/b = 15$, the first six energy levels of the system are calculated and the results are plotted in Fig. (4.3).

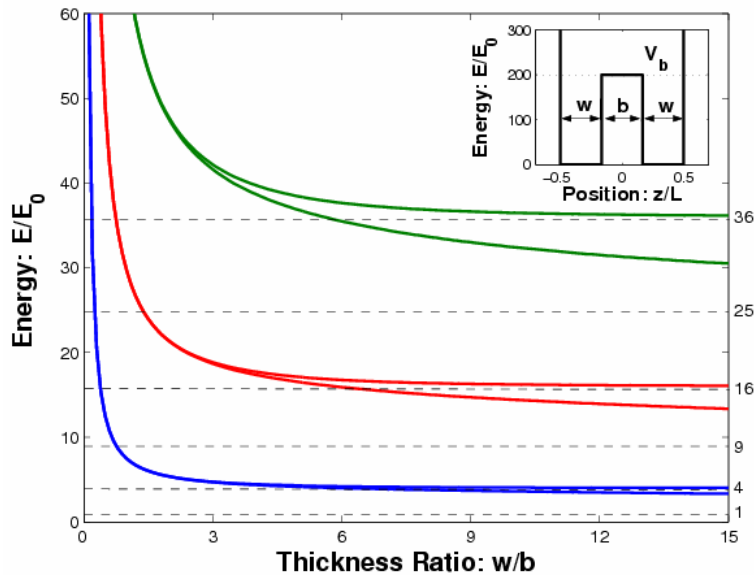


Figure 4.3. First six energy levels of a double quantum well system (see inset) as function of the ratio (w/b) for $V_b = 200E_0$.

The barrier causes a splitting of the energy levels into two states, which collapses into a single degenerate level with decreasing w/b .

For two selected values of the barrier thickness, the first two wavefunctions of the double well system are calculated and the results are presented in Fig. (4.4). In the figure, the solid lines correspond to the first two wavefunctions calculated for the ratio of $w/b = 1$. And dashed lines correspond to the same wavefunctions for the ratio of $w/b = 5$.

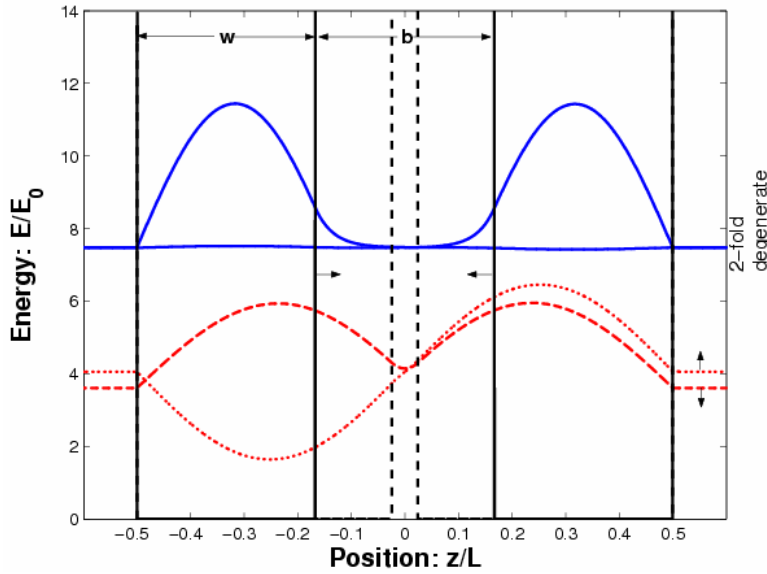


Figure 4.4. The coupling of a symmetric double quantum well for different widths of the barrier between the two wells, here $V_b = 200E_0$.

Notice that for the large value of the barrier thickness, both wavefunctions remain at the same degenerate level (at least they can not be resolved in our scale). And in the barrier region, the tunneling of those wavefunctions appears very weak, i.e., there is no coupling between the two wells. However, thinning the barrier sufficiently leads to an increase of the wave function penetration which results into a strong coupling. For small values of barrier thickness we found a coupled well system resulting in a splitting of the energy levels and a decrease of the energy.

4.5 Band Formation in Superlattices

In this section, more barriers with the same height of $V_b = 110E_0$ and equal thickness ($w/b=1$), are inserted in a finite height quantum well (Notice that, $L = N(w + b) + w$, where N is the number of barriers or the period of superlattice). And the energy levels are calculated for an increasing number of barriers/wells. As the number of barriers increases in the quantum well, the lowest energy levels split into an increasing number of levels and are shifted to higher energies. The number of splitted levels raises proportional with the number of barriers as shown in Fig. (4.5).

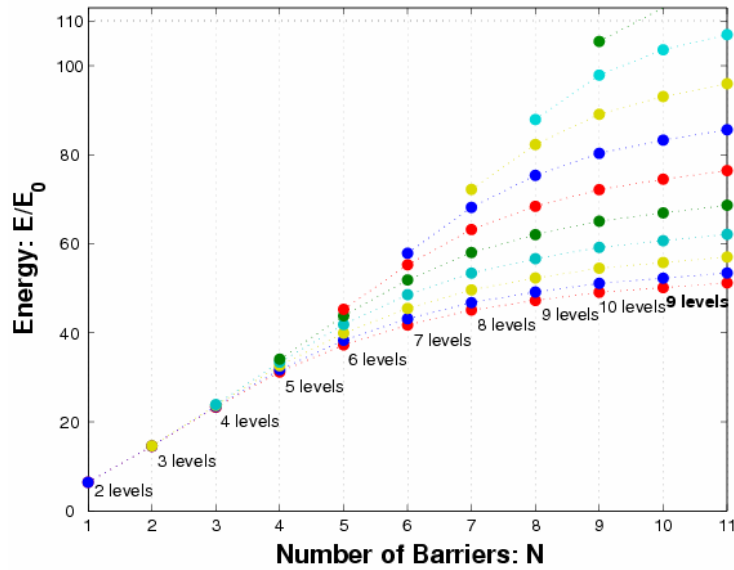


Figure 4.5. The lowest coupled energy levels as function of the number of barriers in a finite single quantum well with $V_b = 110E_0$.

For each increment of the number of barriers, one more level joins to the existing levels. This forms a group of energy levels which for $N \rightarrow \infty$, results in a continuous band. For example, an array composed of 7 barriers, the lowest energy levels split into 8 energy levels. On the other hand, the array composed of 8 barriers contains 9 energy levels. However, for the system including 10 barriers contains 9 energy levels. Because, the 10th and 11th levels are no longer bound due to the finite height of the barriers. For the array with 10 barriers, the first 11 energy levels and corresponding wavefunctions are presented in Fig. (4.6).

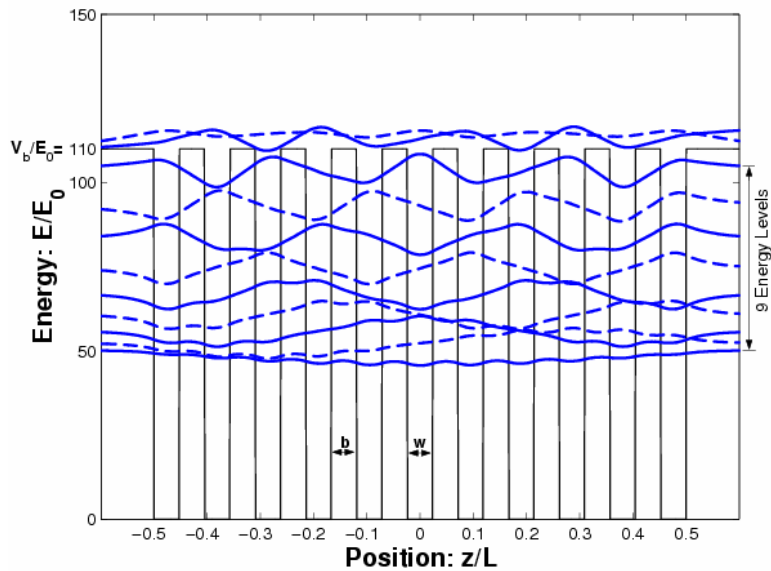


Figure 4.6. First 11 energy levels and corresponding wave functions of the array composed of 10 barriers. The wavefunctions are shifted by their corresponding energy, here $w/b = 1$.

Notice that when the number of barriers increases, the width of the group of all energy levels gets wider and resolves in a band-like structure at higher energy values in comparison with the single quantum well. In addition the wavefunction penetration, i.e., the coupling between adjacent wells becomes more apparent. In the following we will perform the calculations only for the structures composed of 10 or 20 barriers.

4.5.1 Band Formation in a 10-Period Superlattice

In order to form a 10-period superlattice, 10 barriers are introduced in a finite height quantum well. The height of the barriers are taken to be $V_b = 110E_0$. This value of height was chosen after some additional calculations and seemed reasonable in order to observe the formation of the first miniband. The first 11 energy levels are calculated as function of the ration w/b and the result is plotted in Fig. (4.7).

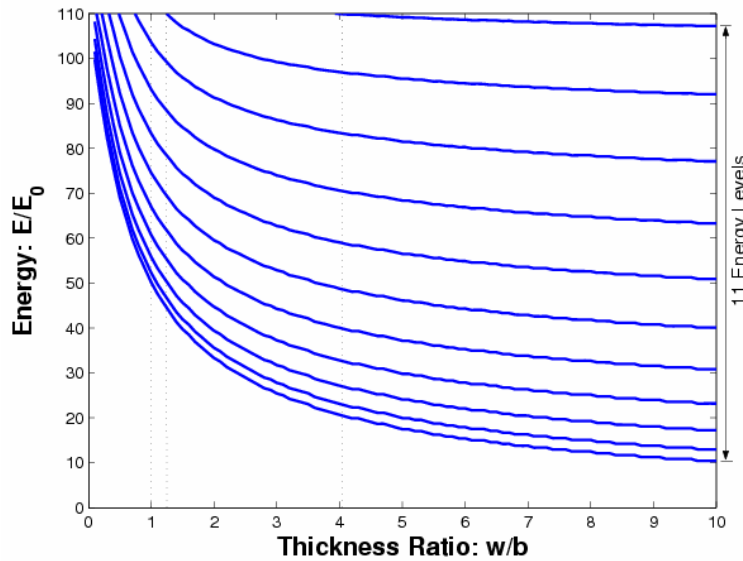


Figure 4.7. First 11 energy levels of a 10-period Superlattice as function of the thickness ratio (w/b) for $V_b = 110E_0$.

For a fixed value of the barrier height and ratio $w/b = 1$, the superlattice contains 9 energy levels in a relatively narrow band. By thinning the barriers (increasing w/b), those levels decrease to lower energy values initially without any increase of the number of bound levels. However, at a certain ratio of approximately $w/b = 1.2$, a 10th energy level appears. Furthermore, thinning the barriers sufficiently up to a ratio of approximately $w/b = 4.0$, the 11th energy level joins to the preceding energy levels. As a consequence of thinning the barriers, the first miniband of the 10-period superlattice tends to appear. Fig. (4.8) shows the new alignment of the first 11 energy levels and the corresponding wavefunctions in a 10-period superlattice for the ratio of $w/b = 8$.

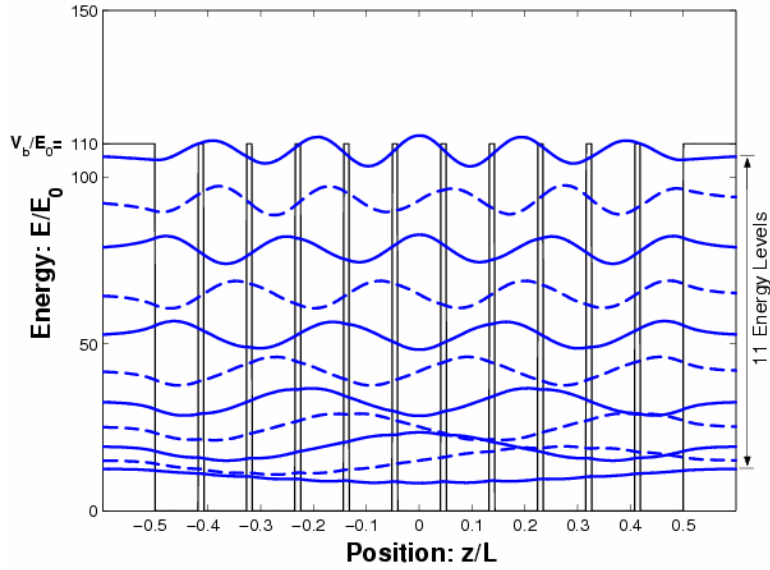


Figure 4.8. First miniband, including 11 energy levels and their corresponding wavefunctions of a 10-period superlattice as function of the position (z/L), here $w/b = 8$.

In order to investigate the situation of the higher energy levels, the height of the barriers is increased to $V_b = 300E_0$. At this particular barrier height, the thicknesses of the barriers are reduced from the value of $w/b = 0.1$ up to $w/b = 10$. And 17 energy levels are calculated by increasing the ratio w/b . The results are presented in Fig. (4.9).

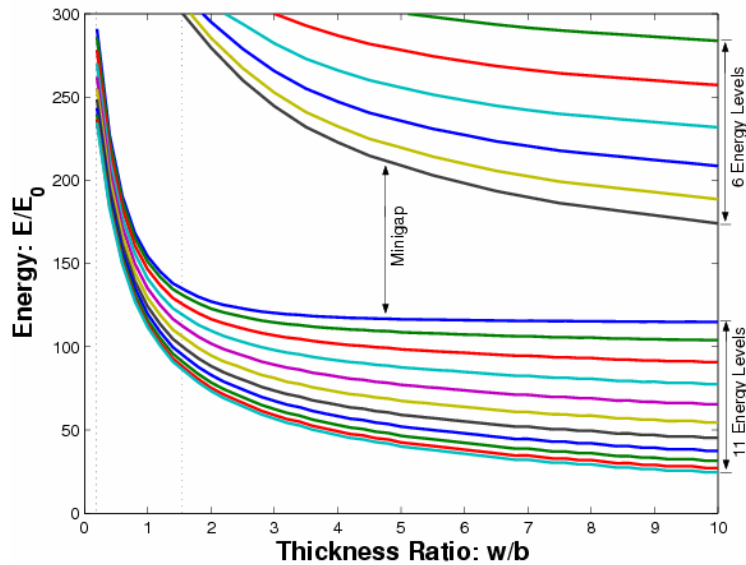


Figure 4.9. First 17 energy levels and formation of the second miniband in a 10-period superlattice as function of the ratio (w/b) for $V_b = 300E_0$.

When the barriers become thinner, the levels decrease in energy. Up to a certain value of approximately $w/b = 1.5$, the superlattice contains only the first miniband including 11 energy levels. However, thinning the barriers further from above this value, the higher

energy levels begin to contribute one by one inside the superlattice array. And this contribution of levels continues as the barriers become narrower.

Well above the upper edge of the first miniband, those higher levels form the second miniband of the 10-period superlattice. In addition, a clear gap (which is the so called minigap) appears between the first and the second minibands. This energy gap is strongly influenced by the change of the superlattice parameters like the potential height and thickness of the layers as well as the period. The size dependence of the minigaps will be discussed in section (4.6).

4.5.2 Band Formation in a 20-Period Superlattice

In this section, 20 barriers with equal thickness are located in a finite depth quantum well. And as it is done in the previous section, the same calculations are performed for a 20-period superlattice. For the height of the barriers $V_b = 430E_0$ and the initial thickness ratio of $w/b = 0.5$, first 21 energy levels are calculated by increasing the ratio w/b . The result obtained from the calculations is plotted in Fig. (4.10).

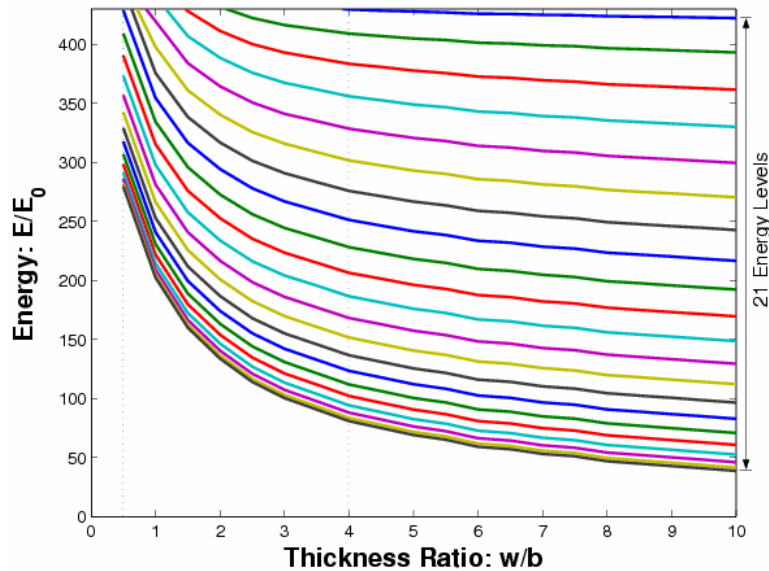


Figure 4.10. First 21 energy levels of a 20-period superlattice as function of the thickness ratio of w/b for $V_b = 430E_0$.

As the thickness of the barriers becomes smaller the energy levels decrease to lower energy values. Initially for the ratio of $w/b = 0.5$, the superlattice contains 14 energy levels in a very narrow band because of the wide barrier. As the thickness of the barriers decreases, more energy levels contribute onto the existing 14 energy levels by making the

band wider. At the ratio of approximately $w/b = 4$, with the contribution of the last energy level (21st level) the first miniband of the 20-period superlattice is obtained.

In addition to those 21 energy levels, for a higher value of the barrier height e.g., $V_b = 1000E_0$, the calculation is performed for more energy levels (31 levels) by raising the ratio w/b from $w/b = 0.1$ to $w/b = 10$. And the result of the calculation is presented in Fig. (4.11).

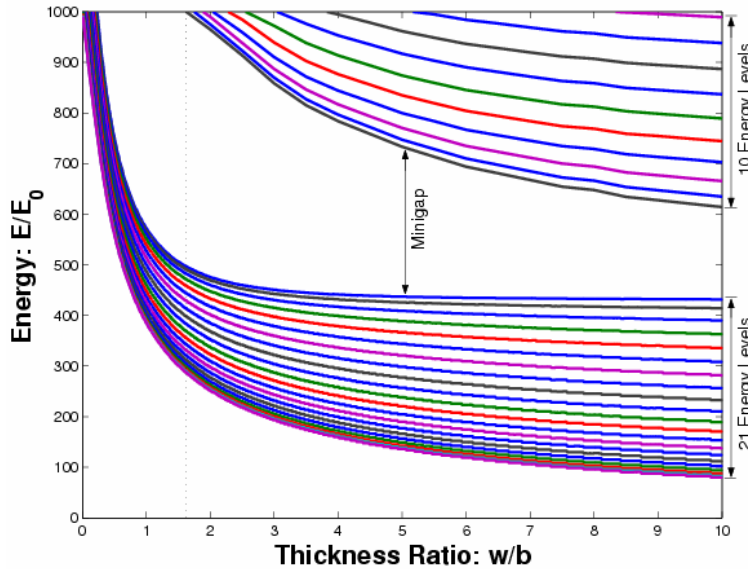


Figure 4.11. The First 31 energy levels of a 20-period superlattice as function of the ratio (w/b) for $V_b = 1000E_0$.

The results exhibit that, for the high value of the barrier height, the first miniband remains very narrow. Initially, from the ratio of about $w/b = 1.5$, the contribution of the higher levels into the superlattice is apparent. These levels take place in a region well above the upper edge of the first miniband. And as the contribution of the upper energy levels continues the second miniband of the 20-period superlattice becomes more apparent with a relatively wide width. In addition, a clear energy gap (minigap) occurs between the 21st and the 22nd energy levels, and this gap is strongly influenced by the change of the barrier thickness as well as the height of the barriers. Fig. (4.11) presents the formation of the second miniband of the 20-period superlattice. And Fig. (4.12) shows the position of the first two minibands and corresponding minigap including the wave functions. Note that, in the plot, the height of the barriers are $V_b = 2000E_0$ and the thickness ratio is $w/b = 2$.

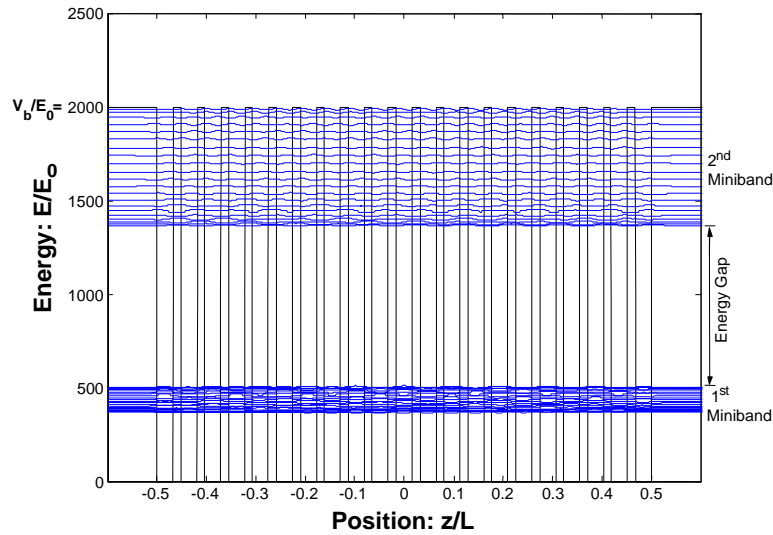


Figure 4.12. The position of first two minibands and corresponding minigap of a 20-period superlattice, here $w/b = 2$.

4.6 Size Dependence of Minibands and Minigaps

In this section the size dependence of the minibands and corresponding minigaps due to the thickness of the barriers will be investigated. Minibands and minigaps are strongly influenced by the change of the barrier and well thickness. In practice, desired width of the minibands and minigaps can be achieved by tuning the thickness of the barrier and well material as well as the height of the barrier potential. By an intelligent tuning of the position, width, and height of this potential barrier, it is possible to close the miniband gap resulting in an order of magnitude enhancement of the miniband width [10].

In order to investigate the size dependence of minibands and minigaps, the calculation is performed on a 20-period superlattice structure. Initially, the energy levels (42 levels) of the 20-period superlattice are calculated by reducing the thickness of the barriers at a constant height. As a result of this calculation, different widths of the first and the second minibands as well as the width of the minigap are obtained. The energy levels of the 20-period superlattice are plotted in Fig. (4.13) as a function of the ratio w/b . The widths of the minibands are calculated for each barrier thickness by taking the difference between the energy levels located at both edges (bottom and upper) of the minibands. And the width of the minigaps is calculated by taking the energy difference between the bottom edge of the second miniband and the upper edge of the first miniband. The results are plotted in Fig. (4.14) as a function of the ratio w/b .

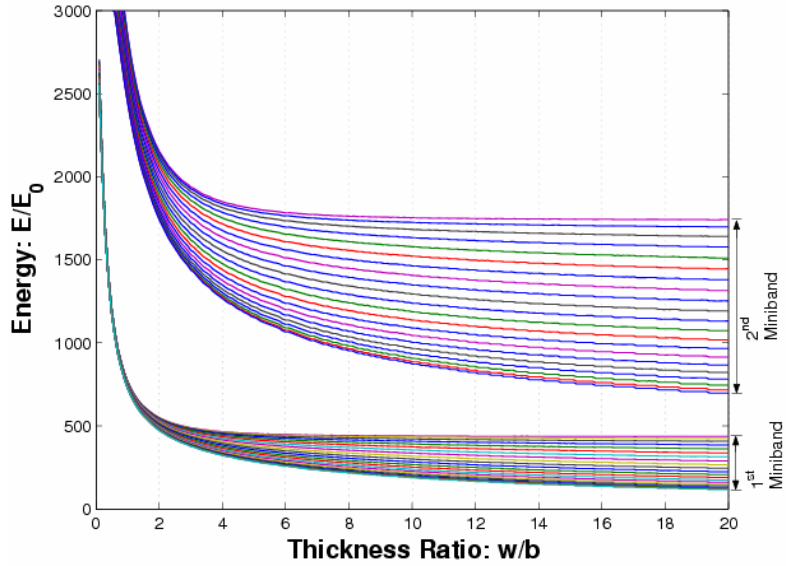


Figure 4.13. First 42 energy levels of a 20-period superlattice as function of the ratio w/b for $V_b = 3000E_0$.

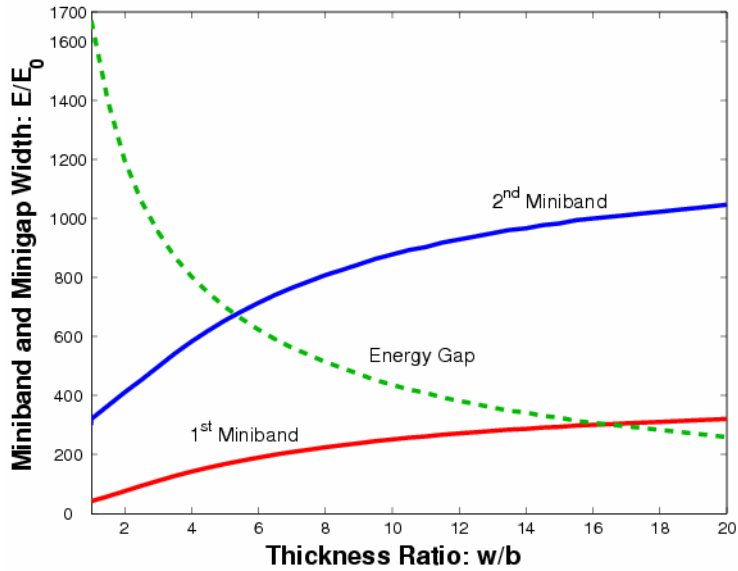


Figure 4.14. The width of the first two minibands and the width of the corresponding minigap as a function of the ratio w/b for $V_b = 3000E_0$.

Our calculations show that, the width of the energy bands can be tuned by varying the thickness of the barriers and/or the thickness of the wells. As the ratio w/b increases the width of both minibands get wider and simultaneously they move closer to each other, hence the energy minigap becomes smaller [see also Fig. (4.17)]. Note that, we obtained the same miniband and minigap behavior when we fixed the ratio w/b and varied the barrier height V_b .

4.7 Formation of Surface/Interface States

Bloch's theorem applies rigorously only to an infinite crystal. But in reality, crystals are not infinite and the validity of this theorem is questionable near surfaces of the crystal, as in the case of superlattice. There may be extra electronic states associated with surfaces that do not obey Bloch's theorem and bear no relation to the band structure of the rest of the crystal; in particular, they may lie near the middle of the band gap. Surface states may also be due to defects and to reconstruction of the atomic surface structure. The behavior of some devices such as FET's is strongly influenced by the high density of surface states.

In order to investigate the formation of the surface states, as a first step, 10 barriers are located in a finite height quantum well. Initially, the height of the quantum well V_0 is taken to be equal to the height of the barriers V_b . And the calculation is done for a fixed height of the barriers $V_b = 500E_0$ and thickness ratio $w/b = 1$. We varied the ratio V_0/V_b , and calculated the 11 energy levels, which form the first miniband. The result is shown in Fig. (4.15).

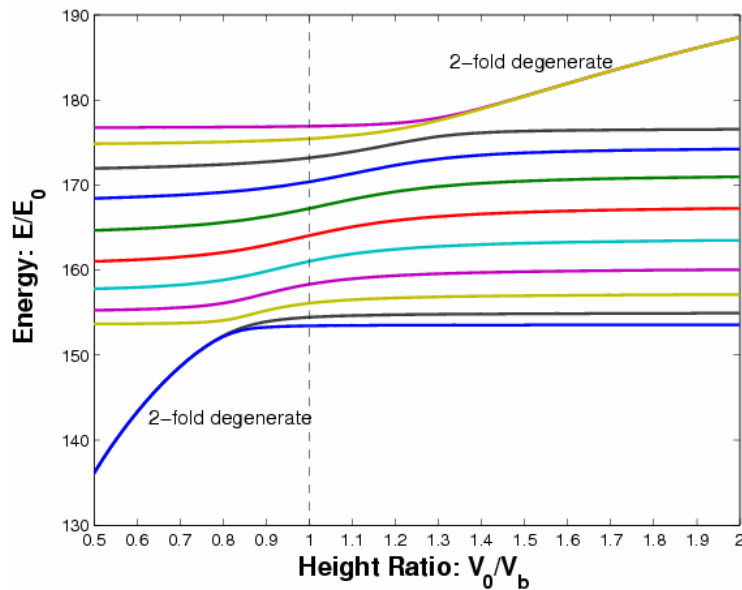


Figure 4.15. First 11 energy levels of a 10-period superlattice as function of the height ratio V_0/V_b , where V_0 is the barrier height outside the superlattice.

Below the ratio $V_0/V_b = 1$, the energy levels of the first miniband tend to decrease smoothly towards lower energy values. Starting from a ratio of approximately $V_0/V_b = 0.8$, the lowest two energy levels separate from the miniband. After a while, those individual splitted levels coincide in energy. Decreasing further the height of the well edges, these two surface states move downward decreasing their energy.

Let us look at the wavefunctions. Without varying any parameter, the calculation is done for the first 22 energy levels and their corresponding wavefunctions of a 10-period superlattice. In the calculation, the barriers with a height of $V_b = 800E_0$ are inserted in a finite height quantum well. The height of the quantum well is taken to be $V_0 = 480E_0$ which yields the ratio $V_0/V_b = 0.6$. The first two minibands and the minigap as well as the surface states are clearly seen in Fig. (4.16). Notice that the surface states appear below the first miniband.

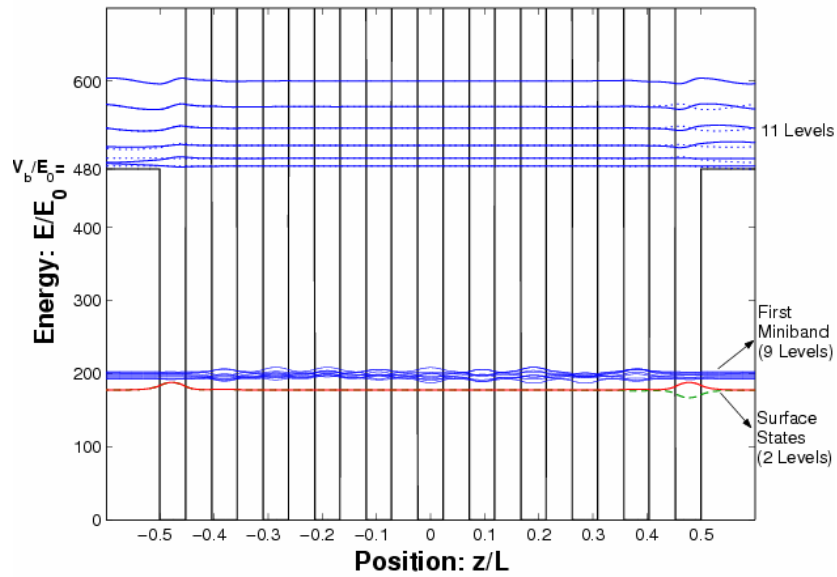


Figure 4.16. First 22 energy levels and the corresponding wavefunctions of a 10-period superlattice with $w/b = 1$, and the ratio $V_0/V_b = 0.6$.

The wavefunctions are only nonzero at the surface (either side of the superlattice), which give these states their nature. The same behavior is observed for the upper two energy levels, but in this case above the ratio of $V_0/V_b = 1$, the energy levels of the miniband increase smoothly in energy. As increasing the height of the well edges, the highest two energy levels separate from their host miniband and again coincide at a ratio of about $V_0/V_b = 1.3$. And they form a very narrow band above the upper edge of the miniband. Increasing the height of the edges further, the two surface states move upward into the energy gap region by increasing their energies.

Again let us look at the wavefunctions. Without varying any parameter, the calculation is done for the first 20 energy levels and their corresponding wavefunctions of a 10-period superlattice. In the calculation, the barriers with a height of $V_b = 800E_0$ are inserted in an infinitely deep quantum well (now $V_0 \rightarrow \infty$) for the ratio $w/b = 1$. The first two minibands and the minigap as well as the surface states are indicated in Fig. (4.17). In this case, the surface states remain well above the first miniband and lay in the gap region.

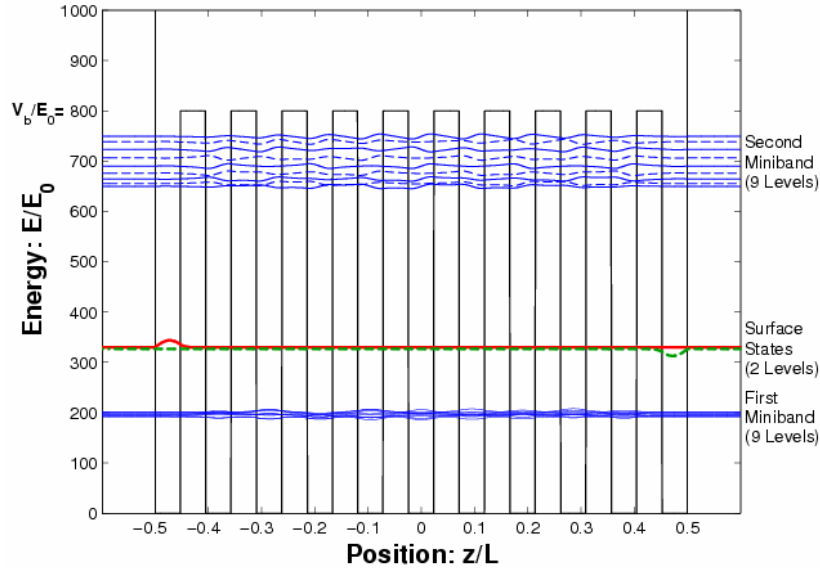


Figure 4.17. The lowest 20 energy levels with their corresponding wavefunctions of a 10 period superlattice with $w/b = 1$, here $V_b = 800$ and $V_0 \rightarrow \infty$.

Compared to the second miniband, the first one is substantially narrower, due to the effects discussed before. In the gap region, well above the first miniband edge the surface states are composed of two energy levels which are very close in energy. Those levels are originated from the splitting of the highest two energy levels of the first miniband as discussed before. Thus, for the 10-period superlattice the first miniband contains 9 energy levels instead of 11 and the surface states contain 2 energy levels. The same situation is observed for the higher minibands with the same reduced number of energy levels. Our further calculations showed that, even by changing the period of the superlattice, the number of surface states between two minibands always remains constant.

Without varying the height of the barriers, as the thickness of the barriers becomes smaller, the surface states move closer to the parent miniband by splitting from their degenerate levels. As the reduction of the barrier thickness continues, the surface states mix with the host miniband. According to these explanations, for three values of the ratio w/b , the band profile of the 10-period superlattice is sketched in Fig. (4.18). This figure shows the position of the surface states (dashed lines) laying in the gap region, and the first two minibands with their corresponding minigap.

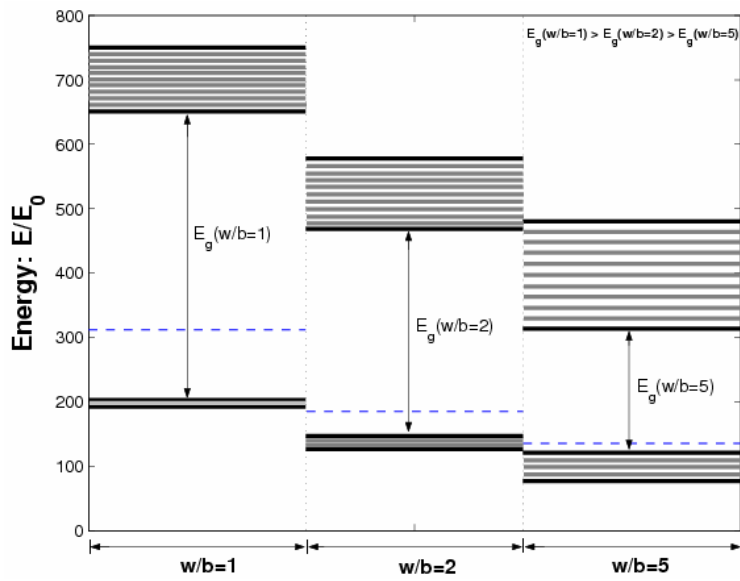


Figure 4.18. The band profile of a 10-period superlattice showing the position of the minibands and the surface states (dashed lines) as function of the ratio w/b .

For a detailed understanding of the surface states, the corresponding wavefunctions of the highest two energy levels of the first miniband are calculated. And the results are plotted in Fig. (4.19) for the same 10-period superlattice in the case of $w/b = 1$.

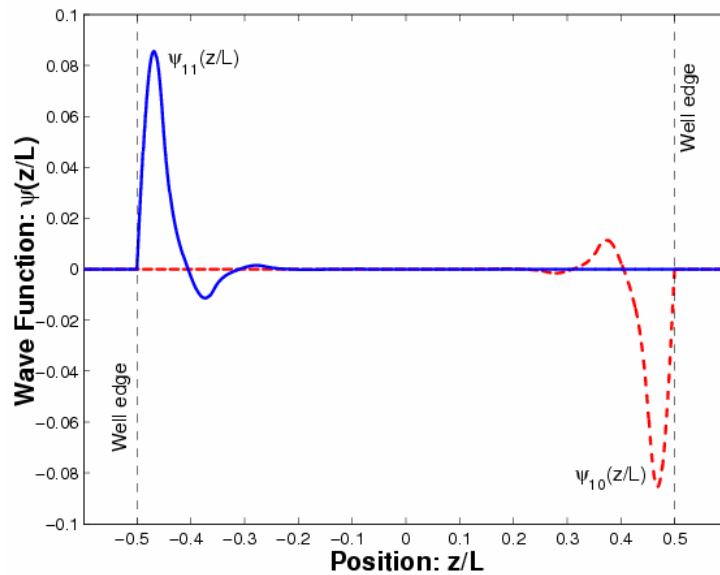


Figure 4.19. Typical wavefunctions of both surface states for $w/b = 1$.

As shown in Fig. (4.19), with respect to the center of the superlattice both wavefunctions exhibit a very clear symmetrical picture. These wavefunctions penetrate into only two barriers/wells by decreasing their amplitude. Towards the inner part of the superlattice both wavefunctions disappear in the well and in the barrier regions. Hence, in comparison with the inner regions of the superlattice, the probability of finding the particles (e.g., electrons) is much higher in the regions near the superlattice edges. That means, they are strongly localized near the interfaces, hence the name surface (interface) states. Both surface states mix when $V_0/V_b \rightarrow 1$, which results into a splitting of their energy.

5. EFFECT OF ELECTRIC FIELD ON SUPERLATTICES

5.1 Quantum Confined Stark Effect

In this section, the effect of a uniform external electric field on both the potential profile and the miniband structure of a superlattice will be investigated.

The classical behavior of a charge q in an electric field \vec{F} is simple; it accelerates the charge uniformly at a rate qF/m , and its motion normal to \vec{F} is unaffected. Unfortunately the picture in quantum mechanics is not so straightforward, mainly because one has to use potentials rather than the field. Let us consider a charge $q = -e$ in a uniform electric field F along the z -axis, so the potential energy will be $qV = eFz$, which increases with z if $F > 0$. As the potential depends only on the position z , the Schrödinger equation can be separated in the usual way and hence one can concentrate on the one-dimensional problem. The one-dimensional Schrödinger equation with the additional electric potential is given by,

$$\left[-\frac{\hbar^2}{2m} \frac{d^2}{dz^2} + V(z) + eFz \right] \psi(z) = E\psi(z), \quad (5.1)$$

where $V(z)$ is the height of the barrier potential.

If we take again E_0 as the energy unit and L as the length unit, then the Schrödinger equation can be defined in dimensionless form as,

$$\left[-\frac{1}{\pi^2} \frac{d^2}{dz^2} + \frac{V(z)}{E_0} + \alpha z \right] \psi(z) = \left(\frac{E}{E_0} \right) \psi(z). \quad (5.2)$$

with the chosen variable $\alpha = \frac{eF}{E_0} L$.

The electric field strongly influences the energy levels of a quantum well by tilting its potential profile.

As a first step, a relatively smooth electric field of $\alpha = 5$ is applied perpendicular to a finite quantum well with a barrier height of $V_0 = 20E_0$. And the first four energy levels and corresponding wavefunctions are calculated. The result is plotted in Fig. (5.1).

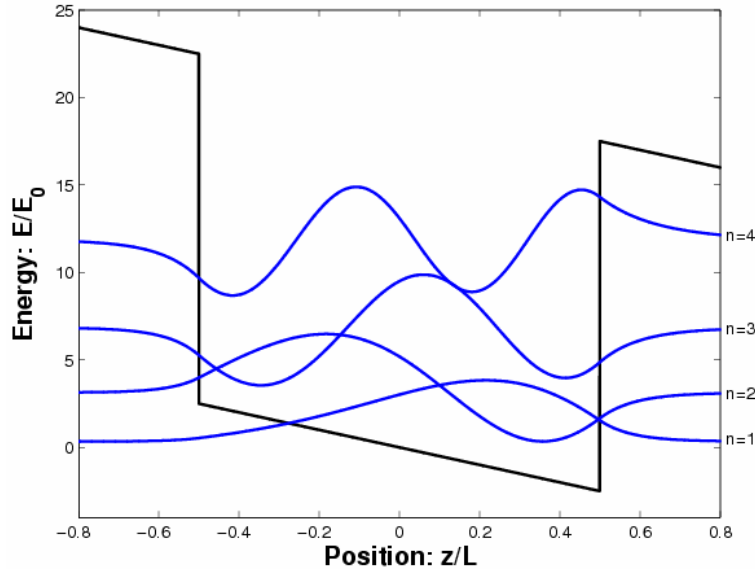


Figure 5.1. First four energy levels and corresponding wavefunctions in the presence of an applied electric field of $\alpha = 5$.

Compared to the finite quantum well studied before, in the presence of a perpendicular electric field, both upper and bottom edges of the well tilts. Depending on the direction of the applied field, one side of the well tilts up and the other side tilts down proportional to the value of the applied field. In addition, as the electric field increases, the lowest level decreases in energy as it sinks into the triangular potential formed in the bottom of the well. Although the higher levels see the same average potential in the well, they are less affected. The applied field thus causes an increase in the separation between the energy level differences ($E_n - E_{ground}$).

In order to observe the effect of the electric field on the energy levels in detail, a quantum well with barrier height of $V_0 = 200E_0$ is considered and a uniform external field is applied perpendicular to the well. The value of the applied electric field is increased from $\alpha = 1$ to $\alpha = 200$. The first 6 energy levels are calculated as a function of the applied field and the result is plotted in Fig. (5.2).

For a relatively weak applied field (e.g., about $\alpha < 5$), mainly the ground state energy is affected while the higher energy states are almost (but not exactly) independent of the field.

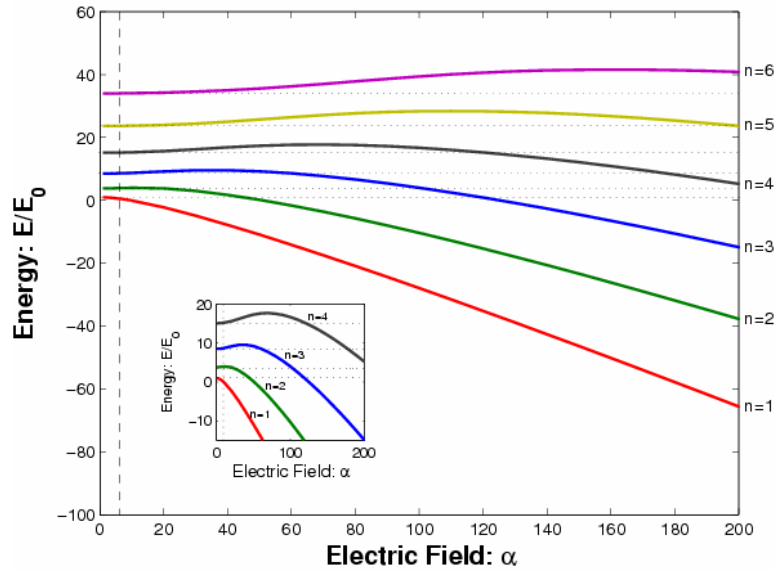


Figure 5.2. First six energy levels of the quantum well as function of the applied electric field. (The inset depicts the small energy range for the lower energy levels)

Increasing the electric field, it is apparent that, all energy levels get apart from their original positions and although the lower energy levels decrease, the higher levels tend to increase smoothly. For a low electric field value, the levels make a ramp and reach a maximum and start to decrease to lower energies. On the other hand, as the field increases, the energy levels get away from each other, thus the whole band gets wider and this yields an increase of the optical excitation energy between the levels. Especially for a finite quantum well, if the electric field is increased strongly, one of the upper edges of the well decreases below the other energy levels, because of the shift of the conduction band. Hence, starting from the highest level, the wavefunctions leak one by one out of the quantum well and the well loses the bound states. Under the influence of a very high electric field, the width of the triangular well can become too narrow, that's why the wave functions can tunnel from the well region to the barrier region (this happens if the height of the barrier is finite). To investigate the typical behavior of the wavefunctions, the typical ground state wavefunction is calculated for three selected values of the applied field and the results are plotted in Fig. (5.3).

As a result of our calculation, we observed that, when an electric field is applied perpendicular to the quantum well, the wavefunction confines in the narrow/deep triangular well and moves along the $+z/L$ direction. And if the field is increased further, the wavefunction hits the well/barrier edge, with a small penetration into the barrier potential.

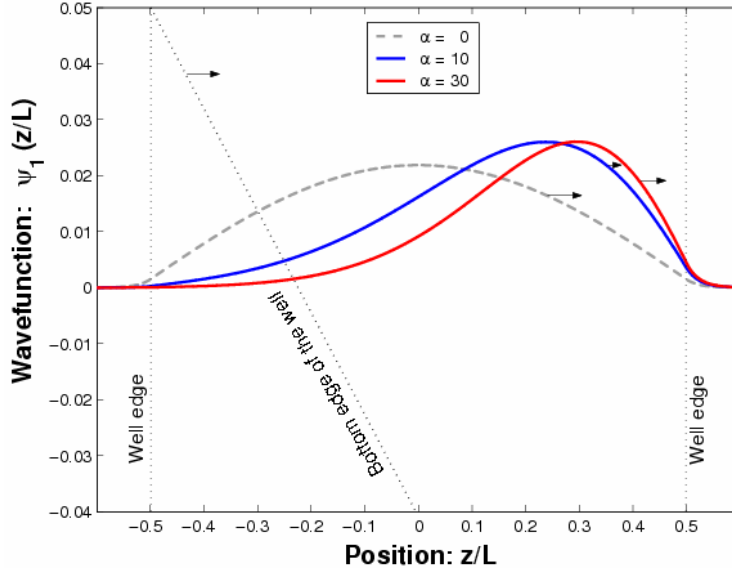


Figure 5.3. Electric field dependence of the ground state wavefunction of a quantum well.

A vertical electric field, applied perpendicular to the layers of superlattice, is known to split up the minibands into a ladder of localized states, the Wannier Stark ladder (WSL). Its existence has been demonstrated through interband optical experiments, involving transitions from the valence to the conduction band [11].

For the case of superlattices, we considered a 10-period superlattice which is located in a finite quantum well. In order to perform the calculation, the height of the barriers is taken to be $V_b = 500E_0$ and the thickness of the barriers is fixed equal to the thickness of the wells, i.e., $w/b = 1$. Under these conditions, a uniform electric field is applied perpendicular to the superlattice. By increasing the value of the applied electric field from $\alpha = 1$ to $\alpha = 250$, the energy levels in the first miniband are calculated and the results are plotted in Fig. (5.4).

For low values of the applied field (e.g., for $\alpha < 5$ in our calculations), although the lowest ($n = 1$) and highest ($n = 11$) levels are strongly affected, all the other energy levels are less affected. Thus, those levels roughly (not precisely) keep their original energy values with a relatively very small energy difference in the first miniband.

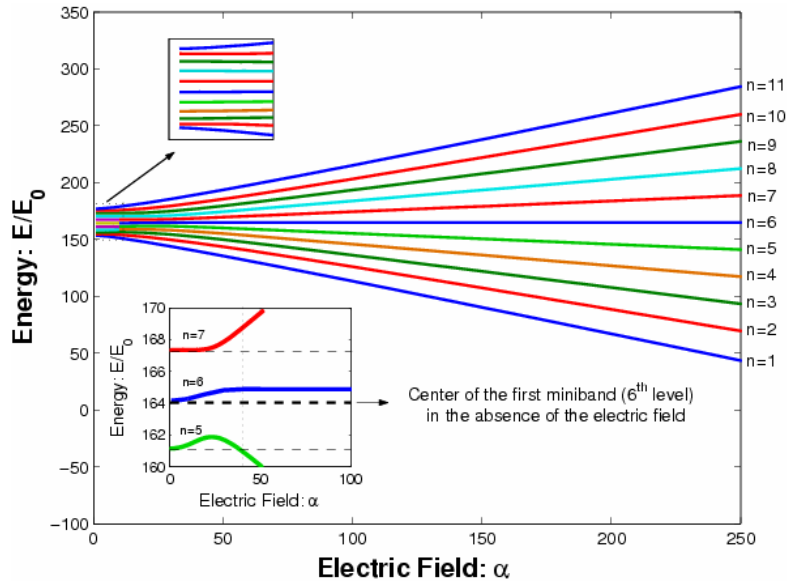


Figure 5.4. First miniband of a 10-period superlattice as function of the applied electric field. (The inset depicts the energy levels $n = 5, 6, 7$ in a smaller field range)

On the other hand, even for weak electric fields, the first energy level suddenly moves away from its original position and decreases in energy. Almost the same behavior is observed for the 11th energy level, however in this case the level climbs upward by increasing its energy. Thus both levels move in opposite directions by the increment of the applied field. As the electric field is increased sufficiently, with respect to the origin of the central energy level ($n = 6$) of the miniband [see inset of Fig. (5.4)], the upper levels suddenly start to increase their energy values. And vice versa, lower levels initially make a smooth ramp until they reach a maximum and afterwards they decrease in energy. On the other hand, the situation for the 6th level is a bit different from the other energy levels. Notice that, the central energy level of the miniband is less affected under the influence of a high electric field. Until the field value of about $\alpha = 40$, the 6th energy level tends to rise, as the field increases, this level almost remains at a constant energy value. Consequently, all levels get away from each other, hence the miniband becomes wider.

For three selected values of applied electric field, the first 11 energy levels and their corresponding wavefunctions of the 10-period superlattice are calculated. In the calculation, the height of the barriers is taken to be $V_b = 500E_0$ and the thickness ratio of wells to barriers is $w/b = 1$. The potential profiles, including wavefunctions are plotted in Fig. (5.5).

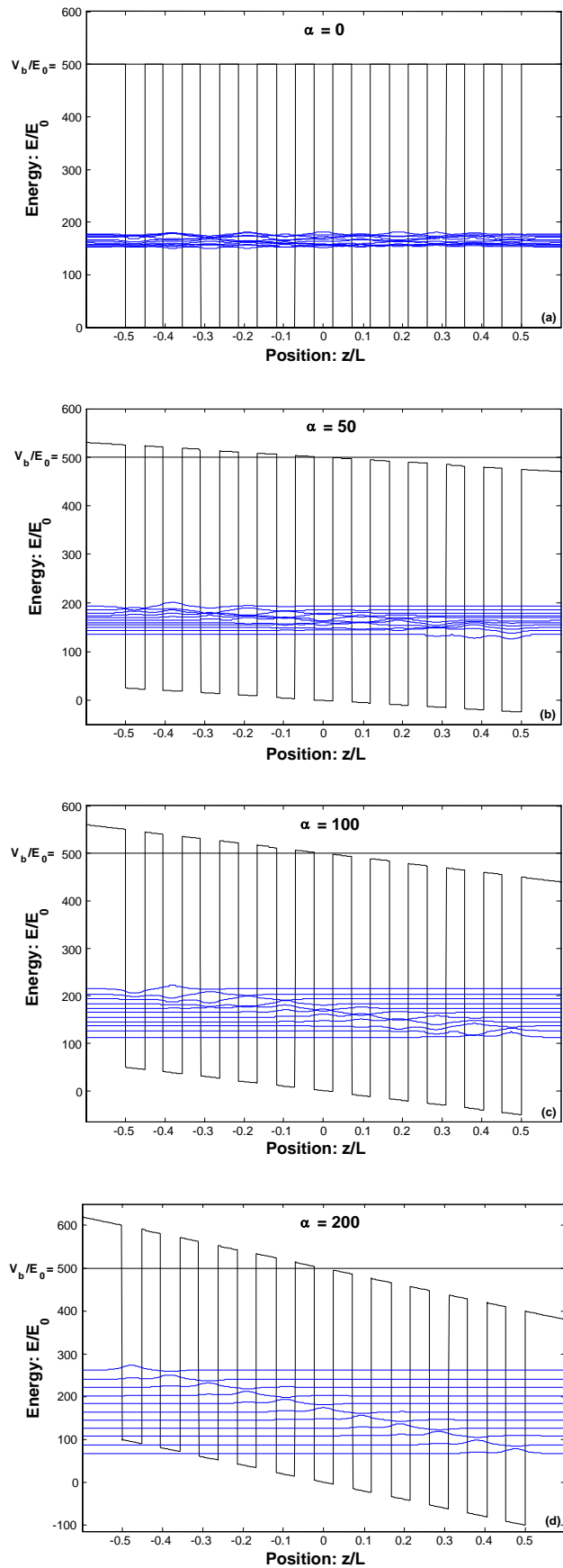


Figure 5.5. First 11 energy levels and corresponding wavefunctions of a

When an electric field is applied, in addition to the shift of the barrier edges, the energy levels get apart from each other. Indeed, the energy spectrum of the miniband splits into a series of levels with a nearly equidistant energy separation at high electric field, which is proportional to the applied electric field. Because of the fact that, the width of the miniband gets wider. Notice, from Fig. (5.5.(d)), for higher values of the applied field, all wavefunctions get localized clearly in the well regions. This clearly indicates a decoupling of the wells. The separation between the energy levels is given by the voltage drop between adjacent wells.

The electric field also influences the second miniband as well as the minigap. To observe the effect of the field on the minigap, a 10-period superlattice is inserted in a finite quantum well with a height of $V_b = V_0 = 1000E_0$. And a uniform electric field is applied perpendicular to the formed superlattice. The first 22 energy levels of the superlattice are calculated and the results are plotted in Fig. (5.6).

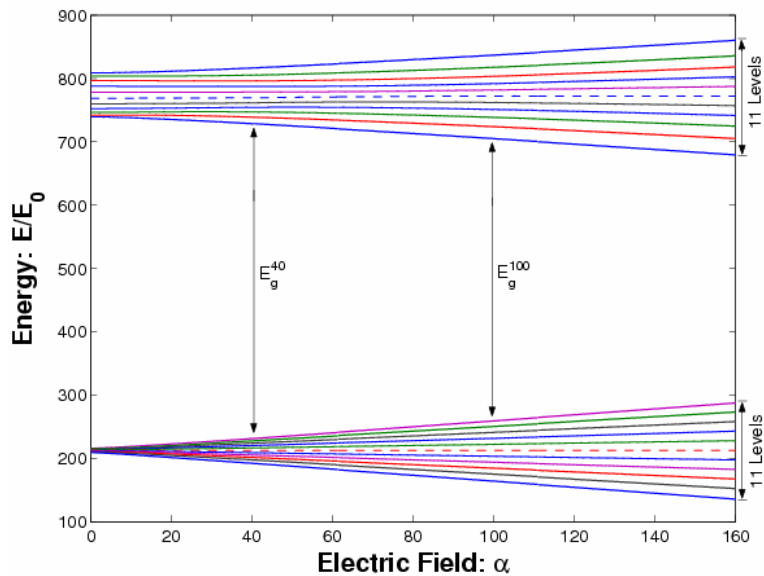


Figure 5.6. First two minibands and corresponding minigap of a 10-period superlattice as function of the applied electric field, here $w/b=1$.

At $\alpha = 0$, the first miniband remains narrower than the second one because of the relatively high barrier height. As the applied field increases, both minibands become wider; the highest energy level (11th level) of the first miniband increases in energy and the lowest energy level (12th level) of the second miniband decreases in energy. Thus, the energy gap, between those minibands becomes smaller (where, $E_g^{100} < E_g^{40}$). On the other hand, the 6th and 17th energy levels of the first miniband and the second miniband (dashed lines) respectively, exhibit a smooth shifting upwards with respect to their initial positions.

5.2 Effect of a Uniform Electric Field on Surface States

In order to investigate the effect of a uniform electric field on the surface states, we formed a 20-period superlattice in an infinite quantum well. For the calculation, the height of the barriers is taken to be $V_b = 500E_0$ and the thickness ratio is fixed to be $w/b = 1$. A uniform electric field is applied on the constructed structure and the field is varied from $\alpha = 0$ to $\alpha = 500$. In the presence of the different applied electrical fields, the first 21 energy levels of the superlattice are calculated and the result is plotted in Fig. (5.7).

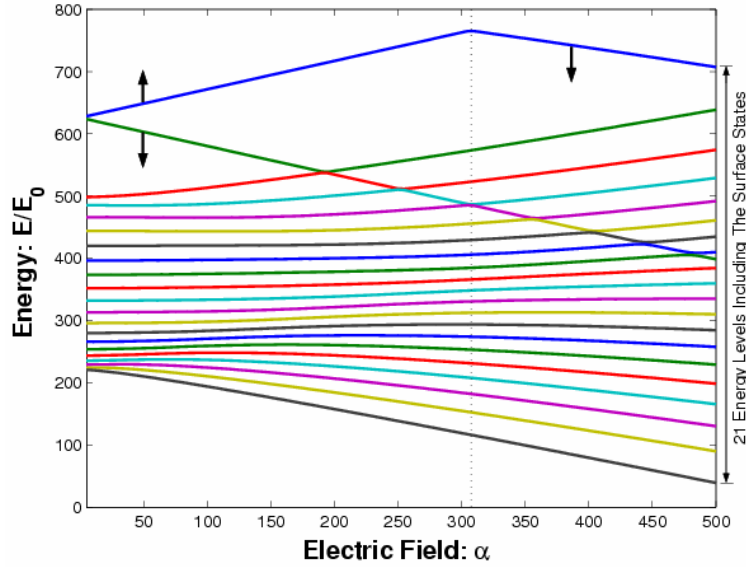


Figure 5.7. First miniband of a 20-period superlattice as function of the applied electric field.

With respect to the center of the miniband, in contrast to the lower levels, the higher levels increase in energy. At certain values of electric field, starting from the highest level an energy breakage occurs due to an anti-crossing through the miniband. And at certain values of electric field, each level suddenly decreases in energy. As the field increases further, the increment of the levels is apparent again. On the other hand, we observed a significant behavior of surface states; as we increase the electric field, the lowest level of the surface states (20th level) decrease in energy, and at a certain value of the field it mixes with the miniband. In short, the electric field pushes down the lower surface state, while it pushes up the other. We found that, as the field increases, the distance between the upper edge of the miniband and the higher surface state remain almost constant. And, at the field value of about $\alpha = 310$, the higher surface state tends to decrease into low energies, and if the electric field increases further it mixes with the miniband. The typical wavefunction behavior of surface states in the presence of a uniform applied electric field is as the same as in Fig. (6.4) of the next section.

6. HETEROSTRUCTURE CONFIGURATION

6.1 Two Dimensional Plane at a Heterojunction Interface

In contrast to the case of three-dimensional electrons in bulk semiconductors, the confinement of electrons in one dimension results in the creation of energy subbands E_i , which leads to the energy spectrum:

$$E_i(\vec{k}) = \varepsilon_i + \frac{\hbar^2}{2m}(k_x^2 + k_y^2). \quad (6.1)$$

Where ε_i is the quantized energy associated with the transverse confinement (confinement perpendicular to the heterostructure). Thus three numbers, one discrete i and the others continuous k_x and k_y , are now associated with each electron state. For fixed i , the continuum range of k spans the energy bands, which is usually referred to as a two dimensional subband. Those bands drastically change some characteristics of the electron system in comparison to the three-dimensional case. For example, in a quantum well, each energy level generates a series of subbands. If the temperature and the electron concentration are such that only the lowest energy level is filled, only free motion of electron is possible in the x, y plane, i.e., in two directions. This system is frequently referred to as a two-dimensional electron gas.

In practice, the confinement of electrons in a two dimensional plane can be achieved by several techniques. The most important one is arguably the modulation doping of heterostructures. We consider a heterojunction of two semiconductors with work functions and bandgaps such that they result in a discontinuity of the conduction band, as indicated in Fig. (6.1.a). Then we assume that the barrier semiconductor material is n doped while the narrow bandgap material on the right hand side of the structure is undoped. In real situations, the latter material is, usually, lightly doped by acceptors, i.e., it is of p -type.

The doped region of the system fixes the position of the Fermi level E_F . At equilibrium, electrons occupy the energy levels up to E_F . Accordingly, the scheme sketched in Fig. (6.1.a) is unstable. The electrons will move toward the undoped crystal until an electrostatic field, brought about by the electric-charge redistribution, bends the band edges so that the Fermi level becomes constant across the material.

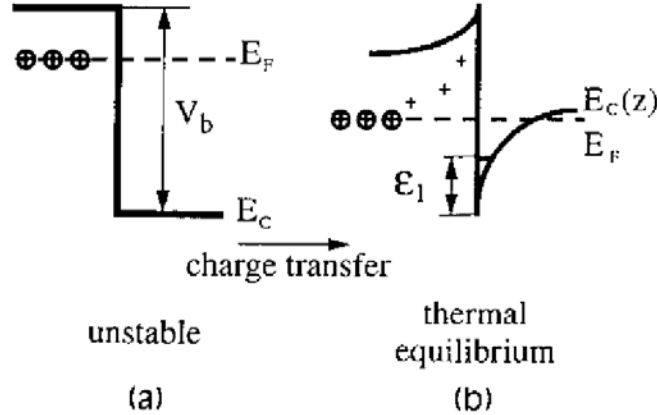


Figure 6.1. Formation of an electron channel at the interface of a single heterojunction, [from V. Mitin, 1999].

Instead of having an energy step, as in Fig. (6.1.a), one obtains the situation shown in Fig. (6.1.b), in which the band edges are bent, there is ionization of impurities in some region of the doped part of the system, and there are free electrons inside the potential well. This well is formed by both the bandgap discontinuity on one side and the electrostatic potential on the other side.

An important conclusion can be derived immediately from this consideration; the bending of the conduction band creates a confining potential for carriers in one direction, say along the z -axis. So there is a quantisation of electrons in the z -direction and so the establishment of a two-dimensional electron gas (2DEG) is realized, at least for very low temperatures.

6.2 Effect of a Nonuniform Electric Field on Superlattices

To obtain a close analogy to the heterojunction type interface potential profile, which is discussed above, a spatially nonuniform electric field is applied perpendicular to a formed superlattice. Because of the nonhomogeneity of the electric field, each of the barriers and wells would see now a different average potential. Thus in comparison with the other regions, one part of the superlattice will have a much higher depth of the potential. The shape of the electric field is discussed below.

The relation given in Eq. (6.2) allows one to vary the lateral shape of the potential profile in superlattice in the perpendicular direction,

$$F(z) = \frac{V_g}{\left[\left(z + \frac{L}{2} \right) + \frac{1}{d} \right]}, \quad (6.2)$$

where L is the total length of the superlattice and can be defined by its period N , and is given by $L = Nb + (N+1)w$, here b and w are the barrier and the well thickness respectively. V_g is the applied potential that determines the strength of the field. And d is an arbitrarily chosen constant which tunes the depth of the potential. This potential is plotted in Fig. (6.2) for three selected values of the potential V_g .

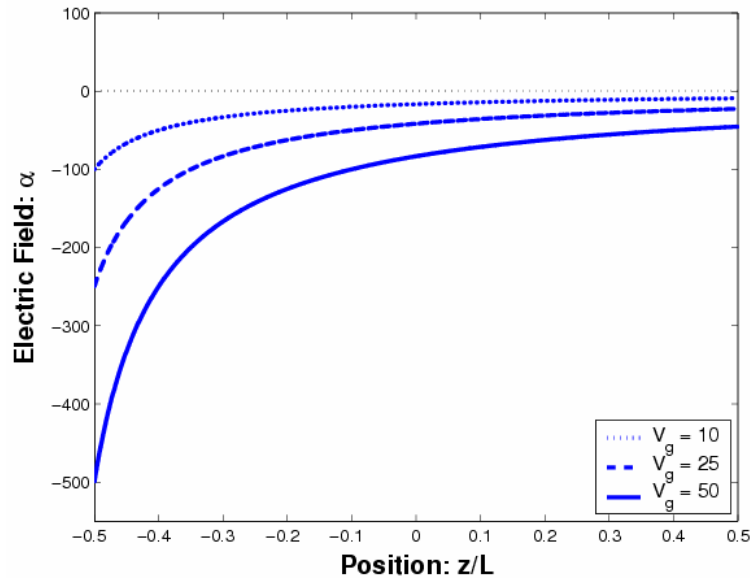


Figure 6.2. The strength of the nonuniform electric field applied to the superlattice for three values of the potential parameter V_g , for $d=10$.

Fig. (6.2) shows how the strength (amplitude) of the field can be varied by the potential V_g for a constant value of e.g., $d = 10$. With respect to the center of the superlattice ($z/L = 0$), this type of the electric field tilts the left side of the structure more than the right side. Hence, exactly at the left edge of the superlattice, a heterojunction type of interface potential can be achieved.

Firstly, a 10-period superlattice with barrier height of $V_b = 500E_0$ is considered in an infinitely deep quantum well. The thickness of the barriers are fixed to be equal to the thickness of the wells, where $w/b = 1$. The nonuniform electric field is applied perpendicular to the system. The potential parameter V_g is varied from $V_g = 0$ to $V_g = 50$ and the 11 energy level of the first miniband are calculated. The obtained results are plotted in Fig. (6.3).

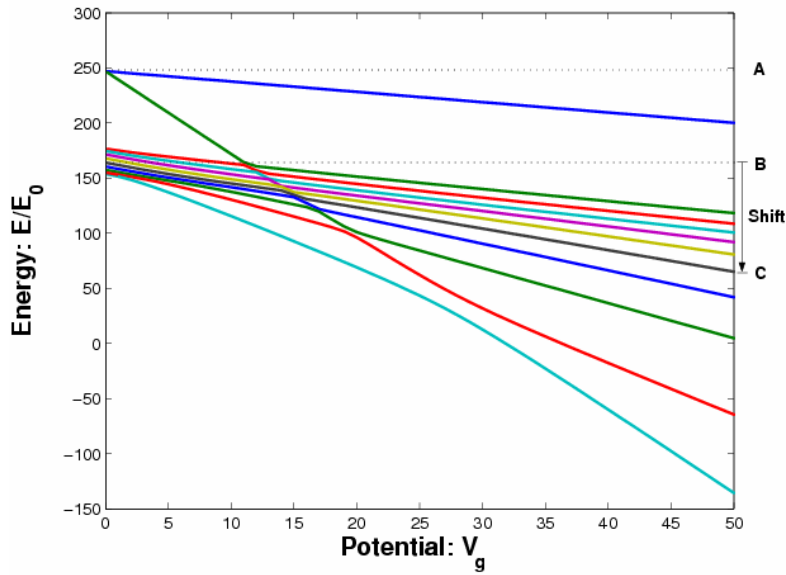


Figure 6.3. The energy levels (including the surface states) of the first miniband of the 10-period superlattice as function of the applied potential V_g .

The nonuniform electric field generated by the potential V_g , strongly influences the energy levels as well as it shifts the miniband from its initial position (B). The energy levels get apart from each other leading to a nonequidistant energy separation between them. Notice that one of the surface states is strongly influenced. As the potential increases, the surface states shift downward from their degenerate position (A). In addition, the lower surface state (10th level) immediately decreases its energy and after a while it mixes with the miniband states leading to an anti-crossing. The other energy level of the surface states (11th level) also decreases in energy; however, roughly it keeps its distance from the upper edge of the miniband. But we found that, if the potential increases further, well above the value of $V_g = 50$, the upper surface state will also mix with the other energy levels of the miniband.

In order to understand this interesting behavior of the energy levels, the corresponding wavefunctions are calculated for the applied potentials ($V_g = 0, 5, 15$ and 50) and the results are plotted in Fig. (6.4).

In the absence of the potential [see Fig. (6.4.(a))], the miniband contains 9 energy levels and the surface states remain in their 2-fold degenerate localized levels at the sides of the superlattice. As the potential is applied Fig. (6.4.(b)), the surface states immediately get apart from each other. The lowest state moves towards the upper edge of the miniband. As the potential further increases, this state mixes with the energy levels of the miniband, at the same time; starting from the lowest level of the miniband the separation of the levels becomes more apparent, hence the miniband gets wider. The states get localized one by one and confined in the well regions. With respect to the left edge of the superlattice, the wavefunction of the first level is localized in the first well, the wave function of the second level is localized in the second well and so on.

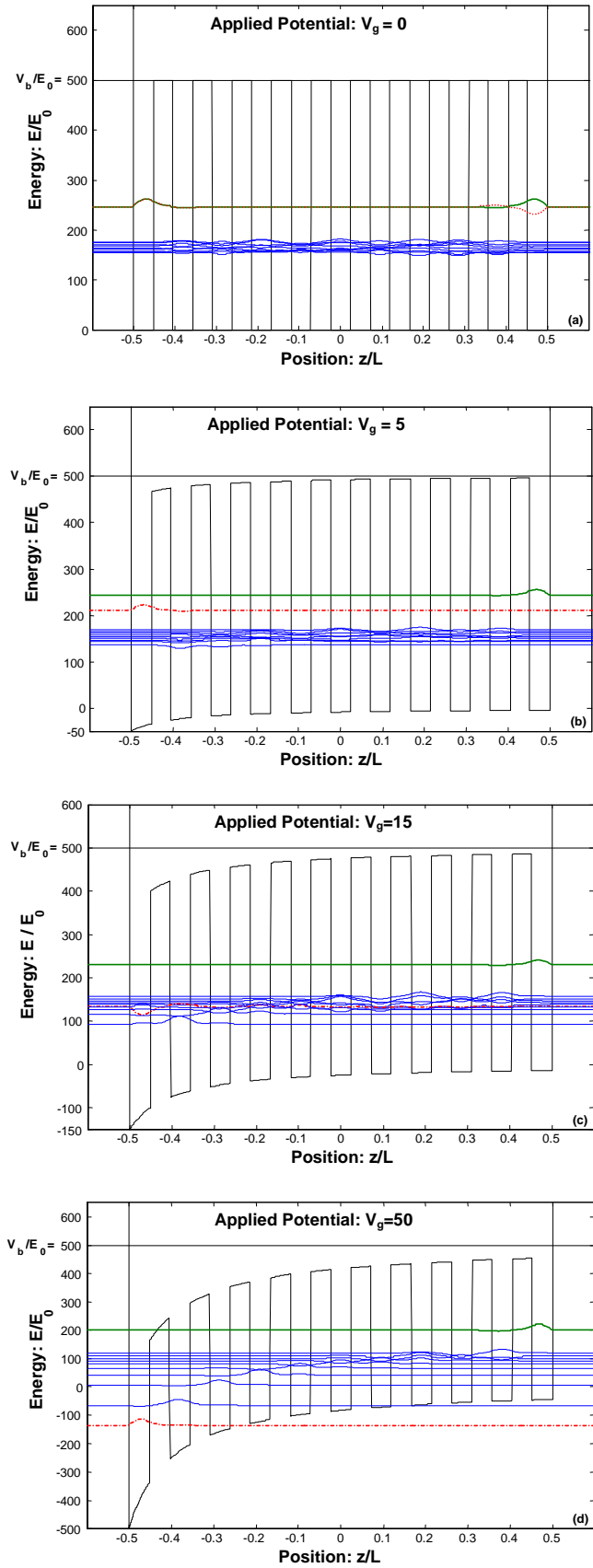


Figure 6.4. The energy levels and corresponding wavefunctions of the first miniband of a 10-period superlattice under the influence of different values for the applied potentials.

7. ELECTRICAL TRANSPORT

7.1 Calculation of the Fermi Energy for a Two Dimensional Band

From the results presented in the previous calculation, it is seen that the electron energy spectrum in a superlattice is complex and consists of a series of energy levels grouped in minibands. The distances between energy levels are determined by the profile of the potential, while the spectrum due to the in plane motion is unaffected. The number of occupied subbands depends on the density of electrons as well as the temperature. The density of electrons per unit area n can be found in the usual way by integrating the product of the density of states $g(E)$ and the Fermi-Dirac occupation function $f(E)$,

$$n = \int_{-\infty}^{\infty} dE f(E) g(E). \quad (7.1)$$

It is convenient to split the density in a sum over the subbands,

$$n = \sum_i n_i \quad (7.2)$$

where n_i is the density of electrons in a two-dimensional band, (including the spin degeneracy), n_i is given by the following form,

$$\begin{aligned} n_i &= \frac{2mk_B T}{\pi\hbar^2} \int_0^{\infty} dE f(E) \theta(E - E_i), \quad (7.3) \\ &= \frac{2mk_B T}{\pi\hbar^2} \ln \left[1 + \exp \left(\frac{E_F - E_i}{k_B T} \right) \right], \end{aligned}$$

where E_F is the Fermi energy, T is the temperature and k_B is the Boltzmann constant. Then the density of electrons per unit area is determined by,

$$n = \frac{2mk_B T}{\pi\hbar^2} \sum_{i=1}^{\infty} \ln \left[1 + \exp \left(\frac{E_F - E_i}{k_B T} \right) \right]. \quad (7.4)$$

The electrons in different subbands behave as though they were in a real two-dimensional system with a single step like density of states. All carriers are stuck in the same state for the motion normal to the confining potential, and cannot move along the z -axis as this would require them to change their state. This limit can be achieved experimentally in a 2DEG.

The Fermi energy can be predicted from Eq. (7.4) for the energy levels E_i of a two dimensional band by varying the density of electrons at a constant temperature T . For numerical calculation of the Fermi energy, it is convenient to represent the variables of Eq. (7.4) in dimensionless units. Thus, the relation, for finite number of energy levels, can be defined as follows,

$$\frac{n}{n_0} - \frac{T}{T_0} \sum_{i=1}^k \ln \left[1 + \exp \left(\frac{(E_F - E_i) T_0}{E_0 T} \right) \right] = 0, \quad (7.5)$$

where $n_0 = E_0(2m/\pi\hbar^2)$ is the density of electrons per unit energy E_0 and $T_0 = E_0/k_B$ is the temperature unit of the system. At constant temperature, for a fixed number of energy levels and the density of electrons n , the root of the non-linear Eq. (7.5) give the corresponding Fermi energy. The Fermi energy of the superlattice with the barrier height of $V_b = 500E_0$ (studied before) is calculated for two values of the temperature. At a fixed applied potential $V_g = 50$, [see Fig. (6.4.d)], the density of electrons is varied from $n = 0n_0$ to $1000n_0$, and the result is plotted in Fig. (7.1).

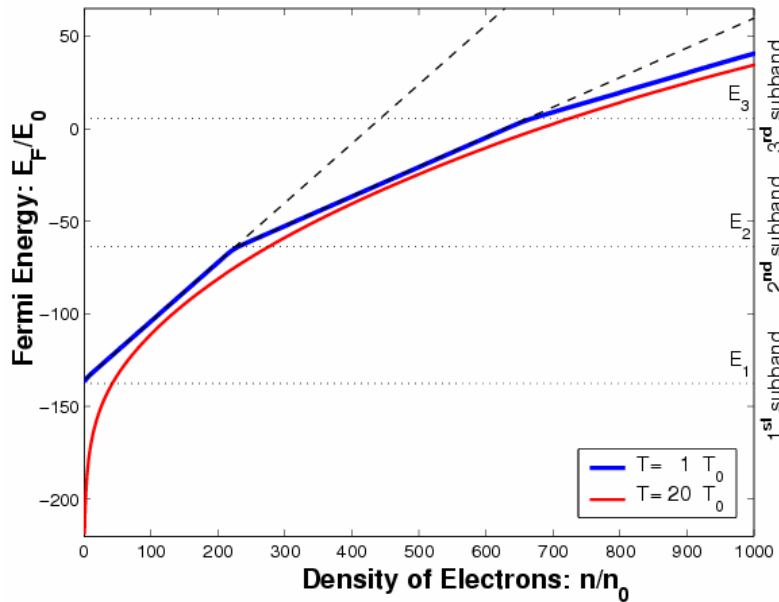


Figure 7.1. Fermi energy as function of the density of electrons for two different temperatures, here $n_T = 1000n_0$.

The previous calculations on our system exhibit that, in the presence of a heterojunction type interface potential, the electron motion perpendicular to the interface is quantized into a sequence of subbands. For low temperatures, if the density of electrons is low (e.g., $n < 220n_0$), only the lowest subband E_1 is occupied. When the density of electrons further increases, the electrons start populating the second subband. Because of this, the Fermi energy exhibits a staircase-shaped electron density dependence, with each step being associated with one of the energy levels at low temperature (e.g., $T = 1T_0$). This two-dimensional nature is somewhat delicate, and quickly disappears if the temperature is raised (e.g., $T = 20T_0$) or if the electrons gain energy from some external source.

7.2 Calculation of Magnetoconductivity of Subbands

The magnetoconductivity of a multi-subband system can be calculated by means of the Shubnikov-de Haas (SdH) oscillations. The Shubnikov-de Haas effect is a suitable technique to investigate the electron transport properties of semiconductors. The amplitude and period of the SdH oscillations depend on the electron density as well as the applied magnetic field. Such that the conductance maximum is reduced and shifted towards a higher density as the magnetic field is increased.

In this section, the transverse magnetoconductivity σ_{xx} of the first and the second subbands, obtained from 10-period superlattice, will be determined from the Shubnikov-de Haas oscillations. At low temperatures, the transverse magnetoconductivity of a system is oscillatory in terms of $1/B$, due to the magnetic quantisation of the electron orbits. If the charge carriers are electrons in the system, including the spin degeneracy, the oscillatory part of the density of states for a particular subband (E_i), can be expressed in the following form,

$$\left(\frac{\Delta g(T)}{g_0} \right)_i = 2 \sum_{s=1}^{\infty} \exp\left(-\frac{\pi s}{\omega_{ci} \tau_i}\right) \frac{2\pi^2 s k_B T / \hbar \omega_{ci}}{\sinh(2\pi^2 s k_B T / \hbar \omega_{ci})} \left[\cos\left(\frac{2\pi s (E_F - E_i)}{\hbar \omega_{ci}}\right) - \pi s \right] \quad (7.6)$$

where g_0 is the density of states without any applied magnetic field, $\omega_{ci} = eB/m_{ci}^*$ is the angular cyclotron frequency, m_{ci}^* is the cyclotron effective mass of the electron in the i^{th} subband at the Fermi level ($E_F - E_i$) and τ_i is the relaxation time of electrons in the i^{th} subband.

And so, the transverse magnetoconductivity for a particular subband E_i , $\sigma_{xx}^{(i)}$ in terms of the oscillatory part of the density of states is as follows,

$$\sigma_{xx}^{(i)} = \sigma_0^{(i)} \left[1 + 2 \left(\frac{\Delta g(T)}{g_0} \right)_i \right], \quad (7.7)$$

where $\sigma_0^{(i)}$ is the conductivity of a particular subband E_i at zero magnetic field, and n_i is the density of electrons in the same subband. Then the total magnetoconductivity of the system is,

$$\sigma_{xx}^{(T)} = \sum_i \sigma_{xx}^{(i)}. \quad (7.8)$$

The Fermi energy is a function of density n_i . For example, at $T = 0K$ we have $(E_F - E_i) = \pi \hbar^2 n_i / m_i^*$ in which the effective mass will cancel out with that of ω_{ci} in the cosine argument of Eq. (7.6). Therefore the frequency of SdH oscillations f_{SdH} , would be simply equal to the two-dimensional density of electrons multiplied by a factor $f_{SdH} = \pi \hbar^2 n_i / e$. If the 2DEG has two populated subbands then the two frequencies interfere and a breathing pattern is observed [see Fig. (7.2)].

According to Eq. (7.6), we predicted a dimensionless expression for the magnetic field unit B_0 , which will be used for the next calculations:

$$2\pi^2 k_B T = \hbar \omega_c, \quad (7.9)$$

where $\hbar \omega_c = eB/m$, and for the temperature unit of T_0 , the unit of the thermal energy can be defined as $E_0 = k_B T_0 = \hbar^2 \pi^2 / 2mL^2$, then from Eq. (7.9) we get,

$$2\pi^2 E_0 = \frac{eB_0}{m} \Rightarrow B_0 = \left(\frac{\pi^4 \hbar^2}{eL^2} \right). \quad (7.10)$$

Based on the previous discussions, a uniform magnetic field B/B_0 is applied perpendicular to the 10-period superlattice. The height of the barriers in superlattice is taken to be $V_b = 500E_0$ with the ratio $w/b = 1$. At a fixed temperature $T = 1T_0$, the applied magnetic field is varied from $B = 0B_0$ to $100B_0$. For the total density $n_T = 1000n_0$, the magnetoconductivity $\sigma_{xx}^{(1)}$ and $\sigma_{xx}^{(2)}$ of the first and the second subband are calculated respectively for the same fixed applied potential $V_g = 50$. The results, including the total magnetoconductivity $\sigma_{xx}^{(T)}$ are plotted in Fig. (7.2).

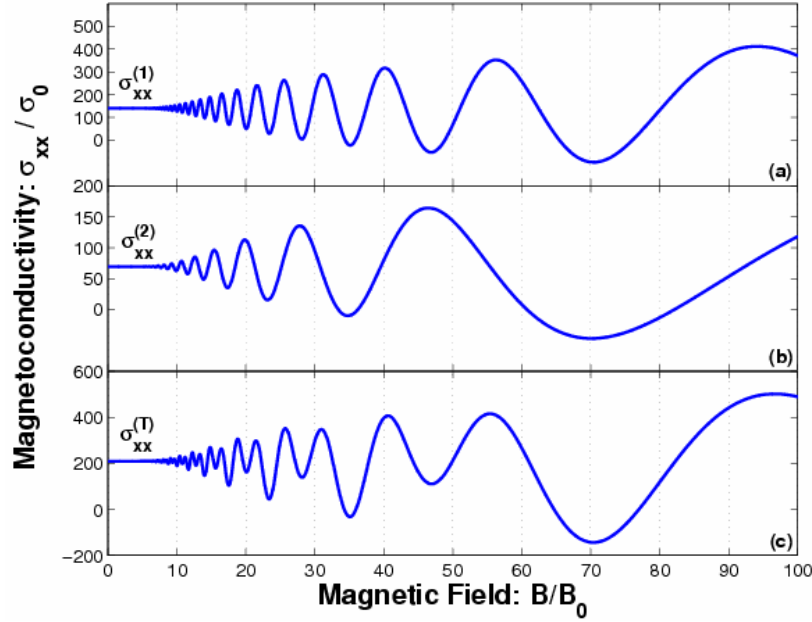


Figure 7.2. Magnetoconductivities of (a) the first and (b) the second subbands (c) the total, as function of the applied magnetic field.

At low magnetic fields (e.g., well below $B < 10B_0$), the conductivity of both subbands don't result in any oscillations (or at least are not resolved). As the magnetic field increases, both conductivities begin to oscillate with relatively low amplitudes and the amplitudes of both oscillations rise proportional to the increment of the magnetic field. Arguably, the most important result of the calculation is that, the magnetoconductivity of the first subband Fig. (7.2.(a)) remains higher than that of the second subband Fig. (7.2.(b)), and with a higher oscillation amplitude. The frequency of both oscillations is also different, so that the SdH oscillation frequency of the second subband is lower than the first subband. This is an expected result because; the electron density of the first subband is bigger than the second one. In other words, in comparison with the first subband, the Fermi level is closer to the second subband rather than the first one, $[(E_F - E_2) < (E_F - E_1)]$. The density of electrons taking place in the first subband gives the largest contribution to the conductivity. In the calculations, it is assumed that both subbands are occupied and the Fermi energy was taken to be $E_F = 4.6E_0$.

8. GRAPHENE BASED ELECTRONICS

8.1 Some Structural Properties of Graphene

Graphene is a single sheet of carbon atoms arranged in the well known honeycomb hexagonal lattice structure that is illustrated in Fig. (8.1). Carbon has four valence electrons, of which three are used for the sp^2 bonds. These electrons define the electronic band structure of graphene that chemists refer to this bond as the π -bond. Notice, there are two such electrons per unit-cell, hence there would be two π bonds per unit-cell. Two primitive lattice vectors \vec{a}_1 and \vec{a}_2 define the lattice structure of graphene;

$$\begin{aligned}\vec{a}_1 &= a_0 \sqrt{3} (1/2, \sqrt{3}/2) \\ \vec{a}_2 &= a_0 \sqrt{3} (-1/2, \sqrt{3}/2)\end{aligned}\quad (8.1)$$

in the (x, y) basis and a_0 denotes the nearest neighbor distance (distance between two carbon atoms) and has the value of $a_0 = 1.42 \text{ \AA}$. The $2p_z$ atomic orbitals are oriented perpendicular to the plane and rotational symmetric around the z -axis.

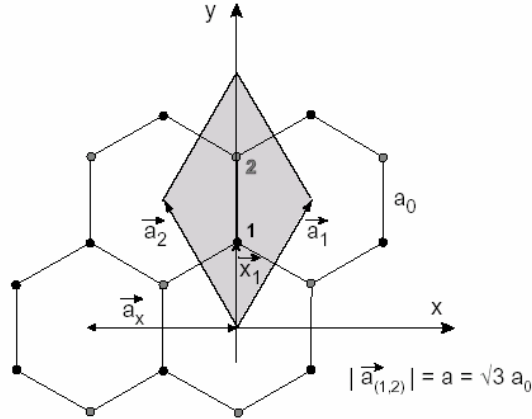


Figure 8.1. Lattice of graphene. Carbon atoms are located at each crossing and the lines indicate the chemical bonds, [from D.R. Lovett, 1977].

The electronic bands of graphene along the high symmetry Γ -K-M and Γ -M directions are shown in Fig. (8.2.b). The electron states are separated into σ and π bands. The π bands can be considered as rising from the overlap of the unhybridized $2p_z$ orbitals normal to the plane. These π bands are very sensitive to the interlayer atomic interactions, which split them into two closely spaced bands. The splitting produces the π (valence) and π^* (conduction) bands which cross at the K point of the Brillouin zone edge. The degeneracy of the bands at the K point gives rise to the semimetallic nature of graphene. On the other hand, the Fermi surface consists only of six distinct points and lies along those crossing points [see Fig. (8.2.a)]. This peculiar Fermi surface is responsible for sometimes metallic and sometimes semiconducting character of carbon nanotubes.

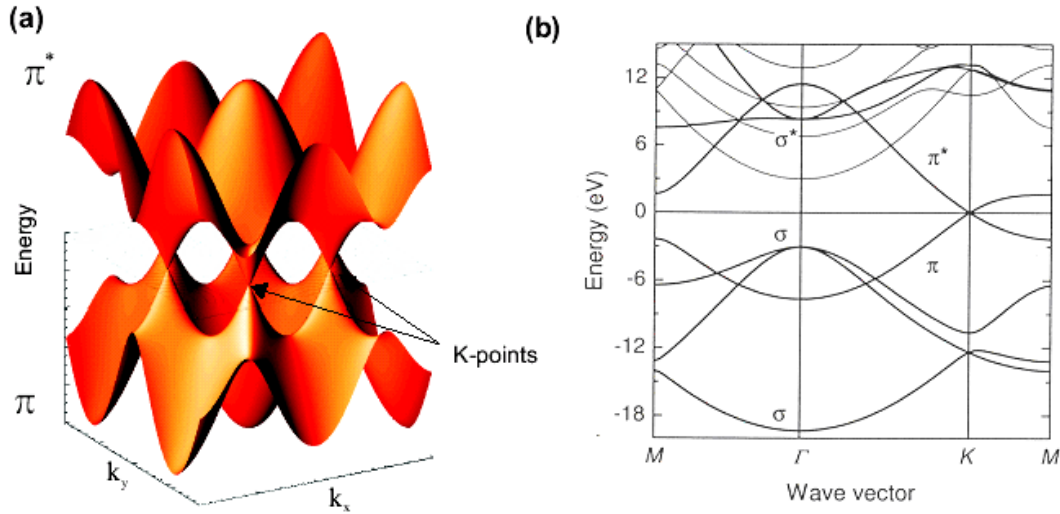


Figure 8.2. The bonding π and π^* anti-bonding orbitals of an isolated graphene sheet. (b) Corresponding electronic band structure. The Fermi level is set to zero, [from S. Reich, 2003].

There is a small energy gap (~ 11 eV) between the bonding σ and anti-bonding σ^* bands at the Γ point. These two do not contribute to many physical effects and are, therefore, often neglected in empirical (e.g., tight-binding) band structure calculations.

The energy band spectrum of the two dimensional graphene is determined by the one electron dispersion relation and can be derived within the tight-binding approximation [12],

$$E(k_x, k_y) = \pm \gamma_0 \sqrt{1 + 4 \cos\left(\frac{\sqrt{3}ak_y}{2}\right) \cos\left(\frac{ak_x}{2}\right) + 4 \cos^2\left(\frac{ak_x}{2}\right)}, \quad (8.2)$$

where $\gamma_0 \approx -2.8$ eV is the C-C interaction energy and $a = a_0 \sqrt{3}$ is the lattice constant of graphene.

8.2 Some Structural Properties of Graphite

Graphite is considered as ‘the prototype’ for the van der Waals bounded solids. It exhibits a well-developed layer structure with strong lattice anisotropy. The electronic properties of graphite are strongly influenced by the anisotropy in the lattice structure. The crystal lattice of graphite consists of an ordered stacking of graphene layers. The stacking order of the layers, as observed in natural graphite, presents two cases of close packed structures: hexagonal and rhombohedral, like in Fig. (8.3.a) and Fig. (8.3.b) respectively.

In hexagonal graphite, the planes are stacked in an *ABAB...* fashion in which the corresponding parameters are given as $a = 2.456 \text{ \AA}$ and $c = 6.696 \text{ \AA}$ (Wyckoff, 1963). The ordering of layers in rhombohedral graphite has an *ABC* sequence. The stacking of planes in graphite is *AB* or, *ABC*, due to the weak interaction between layers derived from the unhybridized $2p_z$ orbitals. This weaker interaction has a spacing of $d \cong 3.35 \text{ \AA}$ between the graphene planes [Reynolds, 1968].

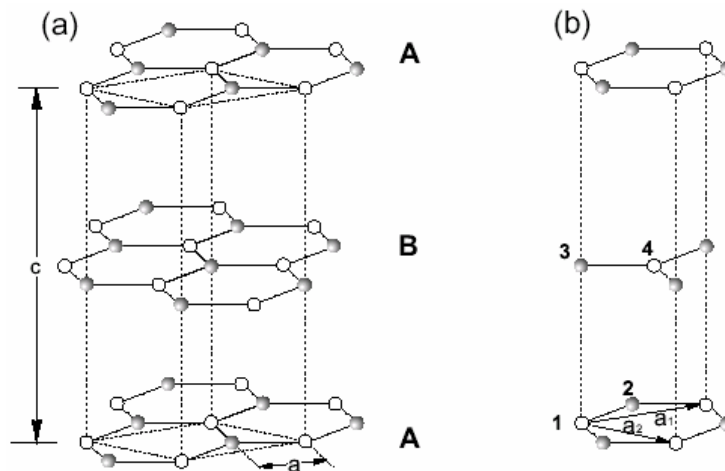


Figure 8.3. Two different closed packed lattice structures of graphite, [from G. Dresselhaus, 2002].

Graphite has four atoms in the unit-cell Fig. (8.3.b) and these four atoms doubles the number of electronic states compared to graphene. Away from the Γ point the electronic bands split because of the doubling. The splitted π and π^* bands overlap at the Brillouin zone edge. Hence, this gives rise to the semimetallic properties and the free electrons in graphite. Note that, two-dimensional graphite is a zero-gap semiconductor and three-dimensional graphite is semimetallic with a band overlap. This band overlap is about 0.04 eV and the band width along the Brillouin zone edge is about $\Delta = 1.56 \text{ eV}$ [15-18]. There are only about 1 in 10^4 free electrons located along the vertical edges of the

Brillouin zone. These location positions are indicated in the diagram of the first Brillouin zone for graphite in Fig. (8.4.a).

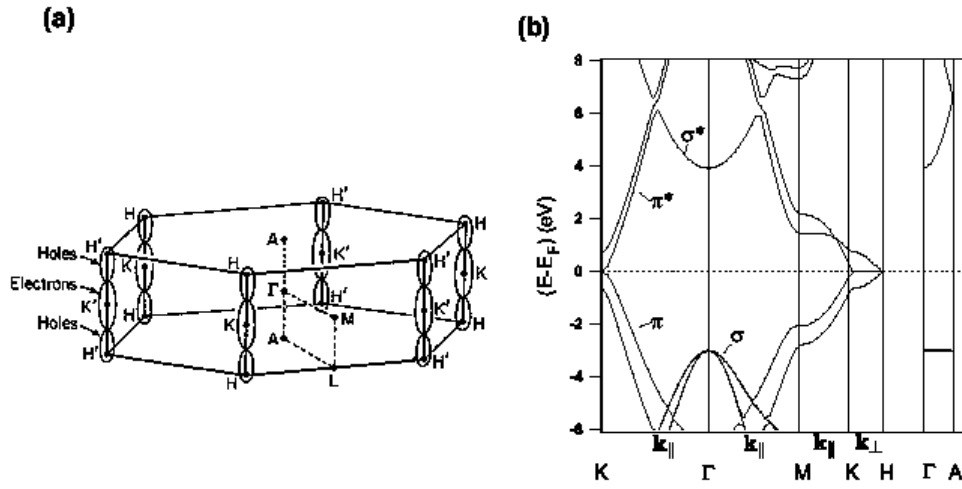


Figure 8.4. (a) First Brillouin zone of graphite with all high symmetry points. And electron-hole Fermi surface located along the HK axes. (b) Corresponding electronic band structure [from G. Dresselhaus, 2002].

The conduction electrons are localized in a two dimensional region between the graphene planes. Within the graphene layer the wave functions are in the form of delocalized Bloch type, while in the c -direction they are localized. The σ -bonds binding the atoms within the planes have maximum charge cloud density in the plane of the C-atoms. The π -bonds are delocalized in two dimensions with maximum cloud density between the planes. It may be that a small potential barrier arising from electron correlation separates the π -electrons in neighboring plane [13].

8.3 Graphene Based Field Effect Transistor (G-FET)

In principle, monocrystalline films of graphite with thickness d down to a few nm sizes can be processed into a transistor-like device (e.g., resistor). Their electronic properties can be controlled by an applied electrical field in such a way that the conduction channel becomes either a high mobility electron or hole gas (2DEG or 2DHG, respectively). The graphene films remain metallic and have a room temperature mobility about $\mu = 15,000 \text{ cm}^2/Vs$ [14-15].

Experiments in Manchester University (by the group of Prof. A.K. Geim), were done on graphene films, which were processed into a multi-terminal Hall bar device placed on top of a SiO_2 substrate [see insets in Fig. (8.5)]. In the experiment, because of their consistent behavior and high mobility, relatively thick ($d \geq 3nm$) graphene films were used. The

films were still sufficiently thin that allowed major changes in their carrier concentration under electric fields $F = 1 \text{ V/nm}$ generated by a gate voltage.

In the experiment, the dependence of the resistivity of graphene films on applied gate voltage (V_g) was measured which is illustrated in Fig. (8.5), where ρ corresponds to the film resistivity per square. One can see that, the resistivity changes by a factor of 4 with varying V_g . The measurements performed in a magnetic field B revealed that changes in the Hall resistivity $\rho_{xy}(B)$ is dramatic [see Fig. (8.5.c)], including a sharp reversal of the sign of the Hall effect as illustrated in Fig. (8.7.b). The observed behavior yields that the electric field doping can transform films of a nominally compensated ($N_e = N_h$) semimetal into either a completely electron or completely hole conductor.

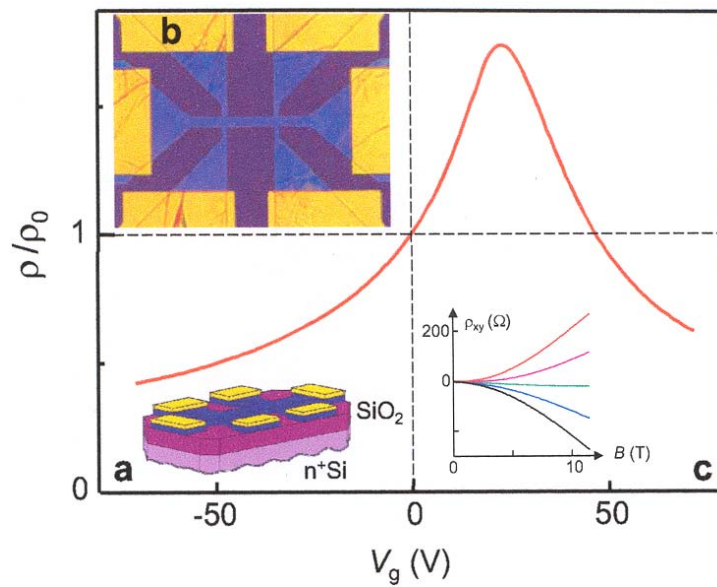


Figure 8.5. The measured field effect in graphene films, [from A. Geim, 2004, ref. (14)].

The main panel in Fig. (8.5) shows a typical dependence of the resistivity of graphene films on the gate voltage at room temperature $T = 300 \text{ K}$. The thickness of the samples used in the experiment was $d = 5 \text{ nm}$ and the resistivity of the samples at zero gate voltage ($V_g = 0$) was about $\rho_0 = 100 \Omega$. Fig. (8.5.a) shows a schematic view of the device and Fig. (8.5.b) shows an optical photograph of one of the devices. Fig. (8.5.c) represents the strong dependence of the Hall resistivity $\rho_{xy}(B)$ on the gate voltage and from top to bottom, the plotted curves correspond to $V_g = -90, -30, 0, 30$ and 90 V . At zero V_g , the $\rho_{xy}(B)$ curve is flat that indicates the case of a compensated semimetal while negative (positive) gate voltages induce a large positive (negative) Hall effect.

The observed changes in the electronic properties of the graphene film as induced by a gate voltage can be understood on the basis of the standard two-band model of graphite [15-16]. With reference to Fig. (8.6), if the Fermi level ϵ_F lies between 0 and ϵ_0 , there are

both electrons and holes present. In this case, the standard two-band model for a semimetal containing electrons and holes describes the metal's conductance σ by [17],

$$\sigma = \frac{1}{\rho} = e(n_e \mu_e + n_h \mu_h). \quad (8.3)$$

where n_e and n_h are the concentration of the electrons and holes respectively and μ_e and μ_h are the respective mobilities.

And the Hall coefficient R_H of the metal is given by,

$$R_H = \frac{(n_h \mu_h^2 - n_e \mu_e^2)}{e(n_e \mu_e + n_h \mu_h)^2}. \quad (8.4)$$

Note that n_e and n_h are not independent parameters but connected so that there is a common value for ϵ_F .

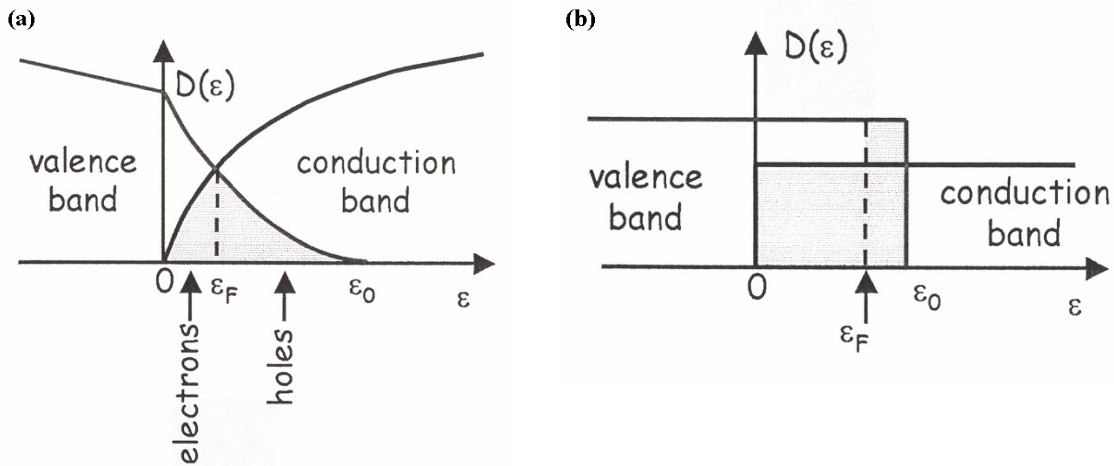


Figure 8.6. (a) The model of density of states in bulk graphite near the K point. (b) The model of density of states for a 2D semimetal, [from A. Geim, 2004, ref. (14)].

If ϵ_F is shifted by doping (electric field doping) below 0 only the holes are left, and vice versa, if ϵ_F is shifted by doping above ϵ_0 only the electrons are left. Thus, instead of a semimetal one can get a completely hole or electron conductor. Then the metal's conductance can be described in the following form,

$$\sigma = n_{e,h} e \mu \quad \text{and} \quad R_H = 1 / e n_{e,h}. \quad (8.5)$$

To calculate the dependence of σ and R_H on V_g (such that ϵ_F varies from well below zero to well above ϵ_0), it is necessary to combine Eq. (8.3) and Eq. (8.5) with the equation for the surface charge density induced by gate voltage given below,

$$n_h - n_e = \varepsilon_0 \varepsilon_d V_g / te = \varepsilon_0 \varepsilon F / e, \quad (8.6)$$

where ε_0 and ε are the dielectric permittivities of free space and SiO₂ respectively, and t is the thickness of the SiO₂ substrate. For $V_g = 0$, the semimetal is compensated with an intrinsic area density of charge carriers $n_i = N_e d = N_h d$. This zero gate voltage yields the compensated state ($N_e = N_h$). The compensated charge density is related to the offset ε_0 (the overlap energy) between the valence and conduction bands through the density of states $D(\varepsilon)$. In the 2D case, $D_{e,h}(\varepsilon) = m_{e,h} / \pi \hbar^2$ ($m_{e,h}$ are the electron and hole masses; the spin degeneracy is 2) and therefore [14],

$$\varepsilon_0 = n_i \pi \hbar^2 (m_e + m_h) / m_e m_h. \quad (8.7)$$

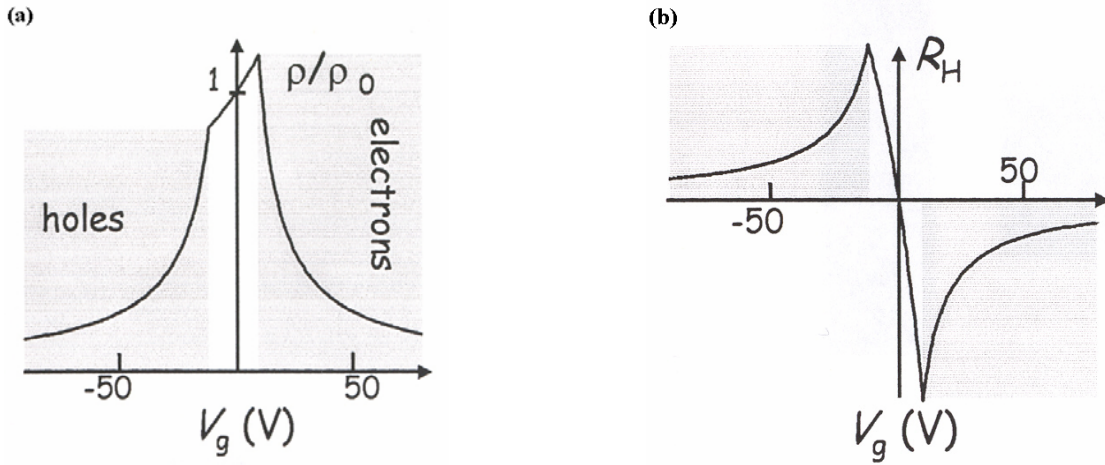


Figure 8.7. The calculated dependence of (a) resistivity ρ and (b) Hall coefficient R_H on applied gate voltage for the 2D case, [from A. Geim, 2004, ref. (14)].

Fig. (8.7.(a)) shows the dependence of ρ on V_g and in the same figure ρ_0 corresponds to the resistivity at zero V_g . At low gate voltages, the resistivity changes linearly with V_g , indicating the substitution of one type of charge carriers by another. At higher V_g only one type of carriers is left and, accordingly, the resistivity follows the standard dependence $\rho = (ne\mu)^{-1}$ for both negative and positive bias voltages. This leads to the characteristic cusp-like shape of $R(V_g)$ -curves. Field doping results in a shift of the cusp region along the voltage axis. Similarly, the behavior of the Hall effect is well described by the same two band model [15-16], Fig. (8.7.(b)). Three regions of electrical field doping (electrons, holes and mixed) are clearly seen on the curves. Close to the compensated state, the Hall coefficient R_H depends linearly on V_g and reverses its sign, reflecting the fact that in the mixed carrier regime R_H is approximately proportional to the difference between electron and hole concentrations. For the voltage regions in which only electrons or holes are left, R_H decreases with increasing the carrier concentration in the usual way, as $1/ne$.

8.4 Application of the Superlattice Model on Graphene Layers

Two basic approaches to calculate the electronic energy bands of a material are the following. One is the tight-binding approximation. According to this approximation the electrons are considered to be part of the atoms forming the solid. Since the atomic distances are very small, the valence electrons in different atoms interact. Because of this interaction the electronic eigenstates broaden and evolve into the continuous bands of a solid. The other approach is based on the Kronig-Penney model. In short, the electrons in a crystal, move essentially as free particles. They feel the periodic potential produced by the atom and interact with the other electrons. This approach describes the electrons as plane waves and starts from the parabolic dispersion of a free electron as shown in Fig. (8.8).

In this section, the model constructed in the previous studies on superlattices and corresponding miniband structure will be applied to layers of graphene. The stacking of graphene layers forms a periodic potential perpendicular to those layers and this situation allows us to treat the electronic bands of graphite by means of the Kronig-Penney model.

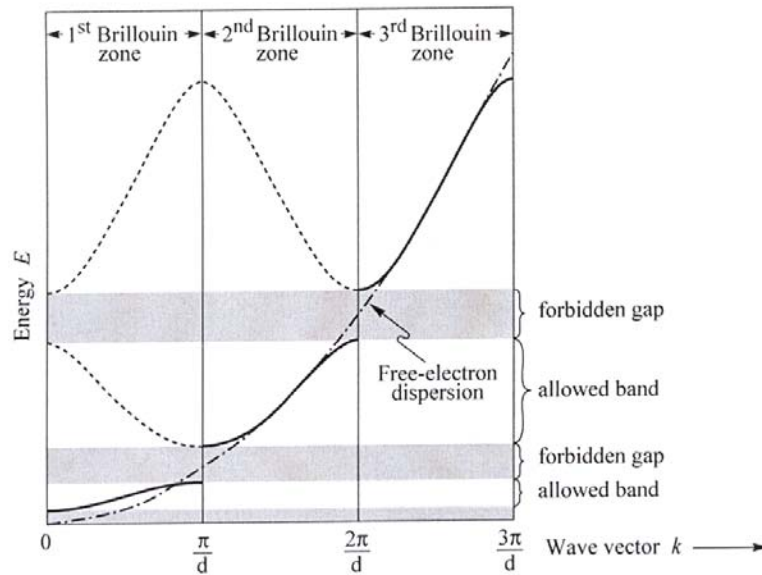


Figure 8.8. Dispersion relation of a one-dimensional lattice of a period d .

The dashed-dotted line represents the dispersion relation of a free electron, [from E.F. Schubert, 2002].

As a first step the height of the potential barriers rising through the electron cloud between the graphene layers is calculated. To imply the problem further we consider the potential barriers as a series of δ -functions which can be defined in the following form,

$$V(x) = \alpha \sum_{j=-\infty}^{\infty} \delta(x - jd), \quad (8.8)$$

where α is the height of the δ -function and $d = (w + b)$ is the period of the potentials. The electron dispersion relation for such a system [similar to Eq. (2.10)] can be written in the following form:

$$\cos(qd) = \cos(kd) + \frac{m\alpha}{\hbar^2 k} \sin(kd), \quad (8.9)$$

where q is the Bloch wave vector (discussed before) and $k = \sqrt{2m\varepsilon}/\hbar$ is the wave number. Along the first Brillouin zone q lies between the points $(0, \pi/d)$, [see Fig. (8.8)]. At $q = 0$, the dispersion relation takes the form:

$$1 = \cos(kd) + \frac{m\alpha}{\hbar^2 k} \sin(kd), \quad (8.10)$$

and this implies

$$\tan\left(\frac{kd}{2}\right) = \frac{m\alpha}{\hbar^2 k} \Rightarrow a = \frac{\tan(x)}{x}, \quad (8.11)$$

where $x = kd/2$, with $x \in (0, \pi/2)$ and $a = m\alpha d / 2\hbar^2$. On the other hand, the band width along the Brillouin zone edges $(0, \pi/d)$ can be expressed in the following form:

$$\Delta = \frac{\hbar^2}{2m} \left(\frac{\pi}{d}\right)^2 - \frac{\hbar^2 k_0^2}{2m} = \varepsilon_{(\pi/d)} \left[1 - \left(\frac{k_0 d}{\pi}\right)^2 \right], \quad (8.12)$$

here $\varepsilon_{(\pi/d)} = \hbar^2 \pi^2 / 2md^2$ is the energy of the electron at the point $k = \pi/d$. In bulk graphite the distance between two adjacent graphene layers is about $d = 3.35\text{\AA}$ and thus the calculated energy is $\varepsilon_{(\pi/d)} = 3.35eV$ (notice, the Planck constant and the free electron mass are taken to be $\hbar = 6.58 \times 10^{-16} \text{ eV}$ and $m_e = 9.11 \times 10^{-31} \text{ kg}$ respectively). We know that the band width along the first Brillouin zone for graphite is about $\Delta = 1.56eV$.

According to the expressions derived above, the wavenumber k_0 and the height of the barriers V_b are calculated. The barrier height is predicted by means of the δ -function approach with the simple relation $\alpha = bV_b$. From Eq. (8.12), the wavenumber is found to be $k_0 = 0.68 \times 10^8 \text{ cm}^{-1}$ for the period of the graphene layers in graphite $d = 3.35\text{\AA}$.

On the other hand, for example, a graphite sample with the thickness of $t = 5 \text{ nm}$ contains 15 graphene layers (which can be considered as the well material). This yields $N = 14$ barriers and the calculated barrier height for $(b = d/5 \Rightarrow w/b = 4)$ is about $V_b = 13.1556eV$.

First, the model obtained from the infinite quantum well is applied to a $t = 5\text{nm}$ thick graphite sample for corrections of energy levels and corresponding wavefunctions. The calculated ground state energy for the system (the energy unit used before) is about, $E_0 = \hbar^2 \pi^2 / 2mt^2 = 15.2 \text{ eV}$. For the same sample thickness, the first six energy levels

and corresponding wavefunctions are calculated according to the infinite quantum well model. The result is plotted in Fig. (8.9).

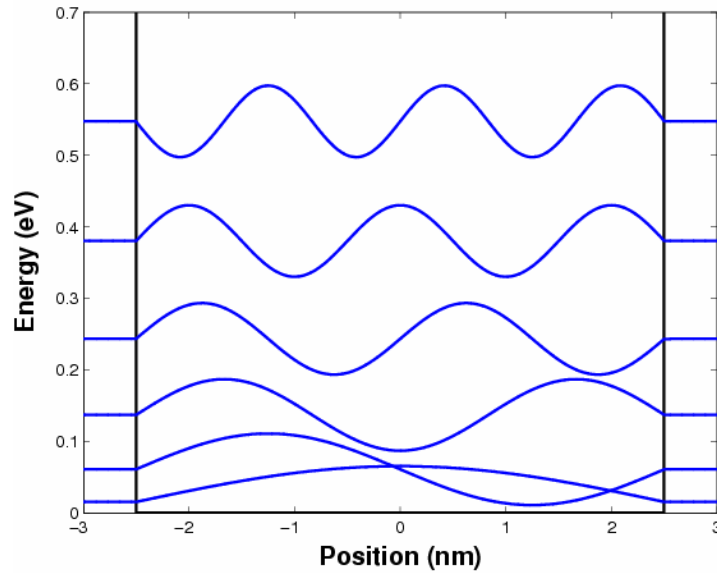


Figure 8.9. First six energy levels and corresponding wavefunctions of graphite according with infinite height barriers at the edge.

It is known that a 5nm thick graphite sample contains 15 graphene layers. Thus, in order to calculate the energy levels in the first miniband, we inserted 14 barriers in the same infinite height quantum well. The height of the barriers is taken to be $V_b = 13.16\text{eV}$ for the ratio $w/b = 4$. We calculated the first 15 energy levels and corresponding wavefunctions and plotted the results in Fig. (8.10).

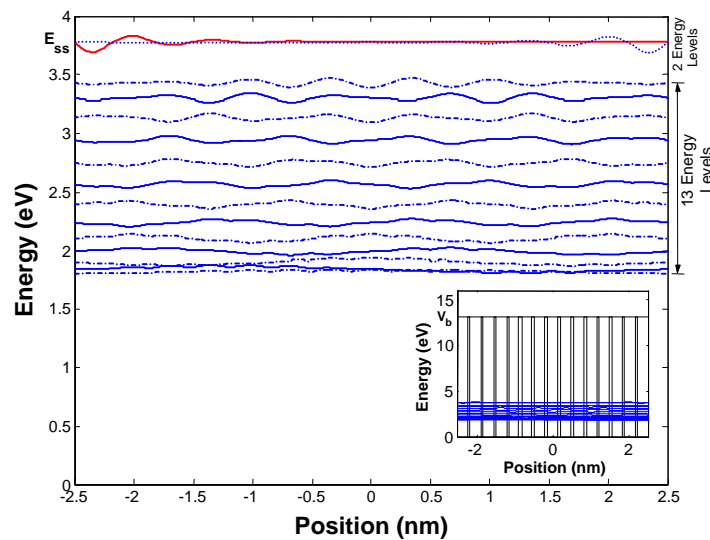


Figure 8.10. First 15 energy levels and corresponding wavefunctions of a 5 nm thick graphite sample composed of 15 graphene layers. The top two levels are the surface states, here $w/b = 4$.

The calculated width of the first miniband, from bottom edge to upper edge (in the region containing 13 energy levels), is about $\Delta_1 = 1.60\text{eV}$. And the surface states are apparent above the upper edge of the first miniband and have a degenerate level of energy about $E_{ss} = 3.78\text{eV}$.

The same calculations are performed for the same number of barriers (15 layer of graphene) inserted in a finite height quantum well. The height of both quantum well and the barriers are taken to be equal with a value of $V_0 = V_b = 13.16\text{eV}$. For the first two minibands, we calculated the first 30 energy levels and corresponding wavefunctions as well as the width of both the first and the second minibands with corresponding minigap. The results are plotted in Fig. (8.11).

According to Fig. (8.11), there are 15 energy levels both in the first miniband and in the second miniband. The calculated value of the width of the first and the second minibands are $\Delta_1 = (3.46-1.82)\text{eV} = 1.64\text{eV}$ and $\Delta_2 = (13.22-7.63)\text{eV} = 5.59\text{eV}$ respectively. And the width of the minigap between those minibands is about $E_g = (7.63-3.46)\text{eV} = 4.17\text{eV}$. In comparison with the exact value of the first miniband width ($\Delta = 1.56\text{eV}$) along the Brillouin zone edge, there is a reasonable deviation from our calculation. The analysis of our results will be discussed in the discussion part of this section.

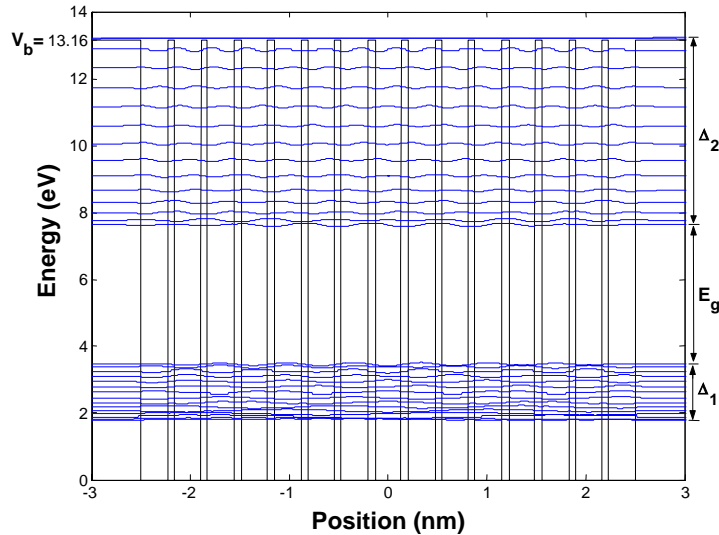


Figure 8.11. First 30 energy levels and corresponding wavefunctions of graphite composed of 15 graphene layers due to the superlattice model, here $w/b = 4$.

We also investigated the effect of a uniform external electric field on the first miniband of a 5nm thick graphite sample. The electric field is applied on the superlattice model of graphite, where the barriers are inserted in an infinitely deep quantum well [see the inset of Fig. (8.10)]. Because of the infinite height of the well ($V_0 \rightarrow \infty$), the surface states are apparent. The calculation is performed for the barrier height $V_b = 13.16\text{eV}$, and the

thickness ratio $w/b = 4$. The applied field is varied from $F = 0\text{V/nm}$ to 1V/nm and we calculated the first 15 energy levels of the first miniband and plotted the results in Fig. (8.12).

With respect to the center of the miniband (at zero applied field), as the applied electric field increases the energy levels are shifted from their original positions. As a result, the miniband becomes wider and an anti-crossing of energy levels is observed. The lower surface state decreases in energy and starts to mix with the energy levels of the miniband at a field value of about $F = 0.12\text{V/nm}$. The calculated width of the miniband at $F = 0\text{V/nm}$ is about $\Delta = 1.6\text{eV}$ and at $F = 1\text{V/nm}$ is about $\Delta = 4.8\text{eV}$. Notice that, up to the field value of $F = 1\text{V/nm}$, there is no contribution of the highest surface state on the miniband; hence the width of the miniband is calculated between the 1st and the 14th energy levels.

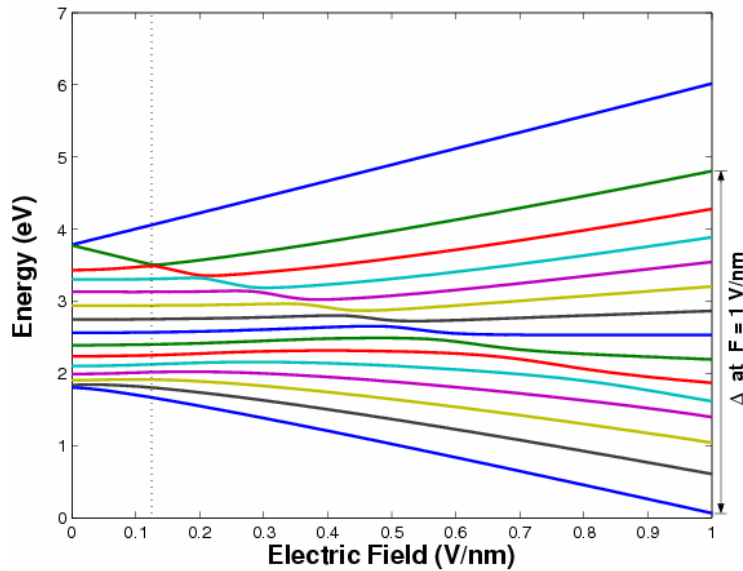


Figure 8.12. First 15 energy levels in the first miniband of a 5 nm thick graphite sample as function of the applied electric field F , here $w/b = 4$.

As a final step a nonuniform electric potential is applied to the superlattice model of graphite. This corresponds probably more to the experimental situation in which a gate voltage is applied. The electric field shifts the carriers to one side of the stack of graphene layers and this redistribution of carriers screens the applied electric field similar to the case of a heterostructure. To obtain the actual shape of the potential we need to solve the Poisson equation and the Schrödinger equation self-consistently. Unfortunately, this is outside the scope of this thesis and therefore we will resort to model potentials as used in the first part of the thesis to model the nonuniform electric potential.

Based on these discussions, the potential barriers are inserted in an infinitely deep quantum well like in the previous study. The height of the barriers is taken to be

$V_b = 13.16\text{eV}$ for the thickness ratio $w/b = 4$. The depth of the potential is increased from $V_g = 0\text{V}$ to $V_g = 2.5\text{V}$. Under these conditions we calculated the first 15 energy levels of the first miniband and plotted the result in Fig. (8.13).

With respect to the center of the miniband in the case of $V_g = 0\text{V}$, the nonuniform applied potential shifts the miniband from its original position (A). From point (A) to point (B) the calculated miniband shifting is about $\Delta E = 4.2\text{eV}$. The width of the miniband at zero potential is about $\Delta = 1.6\text{eV}$ and the width at $V_g = 2.5\text{V}$ is about $\Delta = 2.3\text{eV}$. The contribution of the lowest surface state to the miniband is apparent at a potential value of $V_g = 1\text{V}$. The upper surface state roughly keeps its distance from the upper edge of the miniband while it decreases in energy.

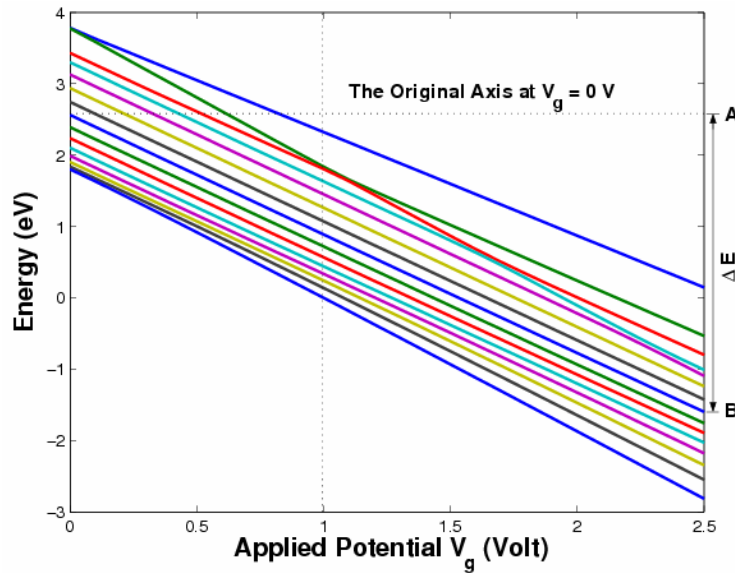


Figure 8.13. First 15 energy levels in the first miniband of a 5 nm thick graphite sample as function of the applied potential V_g , here $w/b = 4$.

By means of the energy levels obtained in the previous calculation, we calculated the Fermi energy E_F of the miniband for an applied potential value of $V_g = 2.5\text{V}$. In our calculation the temperature is taken to be $T = 4.2\text{K}$ and the total density of electrons is varied from $n_e = 0\text{cm}^{-2}$ to $n_e = 1 \times 10^{14}\text{cm}^{-2}$. For the calculation we used Eq. (7.5) and implemented the free electron mass of $m_e = 9.11 \times 10^{-31}\text{kg}$. and the Boltzmann constant $k_B = 1.4 \times 10^{-23}\text{J.K}^{-1}$ into that equation. The result is sketched in Fig. (8.14).

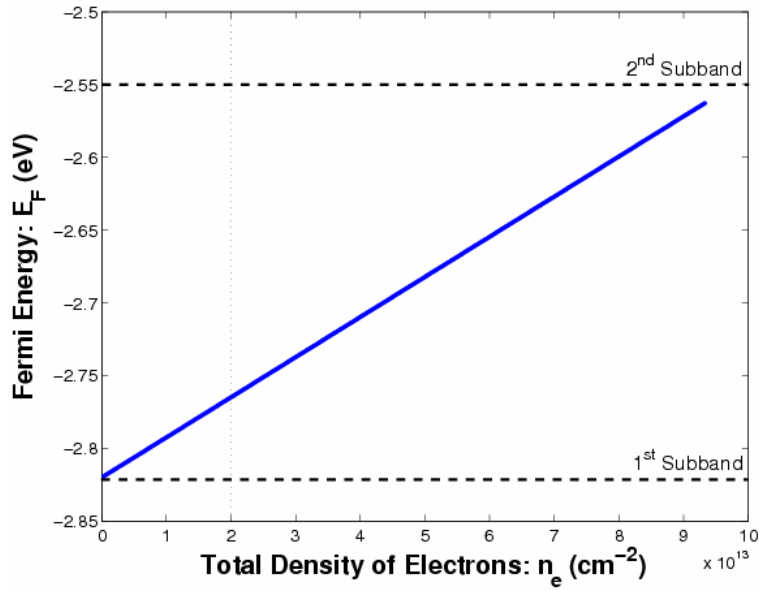


Figure 8.14. The Fermi energy (E_F) of the miniband as function of the total density of the electrons n_e for the temperature of $T = 4.2\text{K}$.

The dashed lines show the bottom of the first and the second subbands. Note that only the first subband is occupied for the total density of $n_e < 1 \times 10^{14} \text{cm}^{-2}$. The experimental results with n_e up to $2 \times 10^{13} \text{cm}^{-2}$ show that only the lowest subband is occupied [14]. Indeed, the result of our numerical calculation which is presented in Fig. (8.14) is in a reasonable agreement with the experimental data. Notice that, similar results can be obtained in the case of the holes.

8.5 Discussion of the Results

As it was discussed previously, for the stacked layers (films) of graphene, the width of the first band along the first Brillouin zone is $\Delta = 1.56\text{eV}$. In our case, the calculated value of the bandwidth of the first miniband is approximately $\Delta = 1.60\text{eV}$. In comparison with the exact value, our result yields a relatively small deviation of about 0.04eV . Note that, more precise results could be obtained by increasing the number of the grid points in our numerical model. However, the further increase of the grid points takes long time in the case of computation and again there would always be small deviations. On the other hand, we have chosen the thickness of the sample to be $t = 5\text{nm}$, which is the same as in the experiment. In the case of the grid points, if we have chosen a different sample thickness we might reduce the stated deviation.

Similar to the experiment, the value of the uniform electric field that we had applied on the superlattice model of the stacked graphene layers, was $F = 1\text{V/nm}$. As a consequence of this field value, in comparison with the situation for the zero field, the energy spectrum of the miniband became wider. And a splitting of surface states was apparent. It is clear that, for specific applications on any device made of graphene films might suffer from the high density of localized surface states. On the other hand, by means of an electric field, the optical and electrical properties of the material can be tuned because of the change of the intersubband energies.

9. SUMMARY AND CONCLUSIONS

In this thesis some important aspects of quantum wells and superlattice structures are studied intensively. This thesis starts with a short description of different energy band diagrams for different semiconductor heterostructures and we showed how superlattices could be grown. The origin of the superlattice band structure is discussed, based on the results of the Kronig-Penney model.

The purpose of this thesis was to make a numerical study of the effect of the finite size of a superlattice on the band formation. Therefore we developed a program to solve the one-dimensional Schrödinger equation for a general external potential, using a finite difference approach. The superlattice structures were modeled by series of barriers. Also the influence of an applied electric field was studied.

From our calculations we observed that the intrinsic behavior of quantum well based structures can be controlled by varying their size parameters (like e.g. barrier width and height). The miniband formation is investigated in detail as function of the width and the number of barriers. An interesting result is the formation of surface states, depending on the height of the confinement potential at the two edges of the superlattice. The two surface states are degenerate and localized near the edges. Their energies can lie in the minigap between two minibands.

Further, we investigated the influence of an electric field on the band structure of superlattices. First we applied a uniform electric field. We studied the field dependence of the bound states and found that an electric field broadens the minibands. We also studied how Wannier-Stark localized states appear. With increasing electric field the wavefunctions get localized in the wells. If the electric field becomes stronger, the number of bound states decreases. An electric field has a strong influence on the energies of the surface states: their degeneracy is lifted, and with increasing field strength, the lowest level can be pushed down from within the minigap through the first miniband and can even become the ground state.

On the other hand by applying a nonuniform electric field, we examined the effect of doping on the minibands. It allowed us to determine the electrical transport properties of our model structure, which might yield many practical applications in the case of nanotechnology.

Graphene is a promising material for future electronics and it has already become a very important base material for many applications. At the end of this thesis, we applied our superlattice model to stacked layers of graphene. We discussed the possibility of a new generation field-effect transistor based on stacked layers of graphene. Therefore we gave a brief overview of its energy band spectrum and compared the results with some experimental measurements. The effect of electric field doping is also discussed. At low and constant temperature, the field doping results in shifting the Fermi level. Within the specified experimental conditions, it is observed that only the first subband is occupied, and this situation can also be observed for holes.

REFERENCES

- [1] C.D. Dimitrakopoulos, D.J. Mascaro, Organic Thin-film Transistors: a review of recent advances. *IBM J.Res. & Dev.* **45**, 11-27 (2001).
- [2] C.H. Ahn, J.M. Triscone, J. Mannhart, Electric Field Effect in Correlated Oxide Systems. *Nature* **424**, 1015-1018 (2003).
- [3] S.J. Tans, A.R.M. Verschueren, C. Dekker, Room-temperature transistor based on a single carbon nanotube. *Nature* **393**, 49-52 (1998).
- [4] S.J. Wind, J. Appenzeller, P. Avouros, Lateral Scaling in Carbon Nanotube Field-Effect Transistors. *Phys. Rev. Lett.* **91**, 058301 (2003).
- [5] S. Rosenblatt, Y. Yaish, J. Park, J. Gore, V. Sazanova, P.L. McEuen, High Performance Electrolyte Gated Carbon Nanotube Transistors. *Nano Lett.* **2**, 869-872 (2002).
- [6] J.H. Davies, *The Physics of Low Dimensional Semiconductors* (Cambridge University Press, Cambridge, 1998).
- [7] P. Vasilopoulos, F. M. Peeters, D. Aitelhabeti, Quantum Tunability of Superlattice Minibands. *Phys. Rev. B* **41**, 10 021 (1990).
- [8] G.T. Einevoll, P.C. Hemmer, Superlattice Minibands—Explicit Formulae for Band Gaps and Effective Masses. *Semicond. Sci. Technol.* **6**, 590-594 (1991).
- [9] V.V. Mitin, V.A. Kochelap, M.A. Stroschio, *Quantum Heterostructures* (Cambridge University Press, Cambridge, 1999).
- [10] F.M. Peeters, P. Vasilopoulos, New Method of Controlling the Gaps between the Minibands of a Superlattice. *Appl.Phys.Lett.* **55**, 11 (1989).
- [11] H. Helm, W. Hilber, G. Strasser, R. DeMeester, F.M. Peeters, Minibands and Wannier-Stark Ladders in Semiconductor Superlattices Studied by Infrared Spectroscopy. *Brazilian Journal of Physics* **29**, 652 (1999).

- [12] S. Reich, C. Thomsen, J. Maultzsch, *Carbon Nanotubes* (Wiley-Vch Verlag GmbH & Co., Darmstadt, 2004).
- [13] D.R. Lovett, *Semimetals & Narrow-Bandgap Semiconductors* (Pion Limited, London, 1977).
- [14] K.S. Novoselov, A.K. Geim, S.V. Morozov, S.V. Dubonos, Y. Zhang, D. Jiang, Room-temperature Electric Field Effect and Carrier-type Reversal in Graphene Films. (unpublished).
- [15] M.S. Dresselhaus, G. Dresselhaus, Intercalation Compounds of Graphite. *Adv. Phys.* **51**, 1-186 (2002).
- [16] I.L. Spain, Electronic Transport Properties of Graphite, Carbons, and Related Materials, in *Chemistry and Physics of Carbon* (Marcel Dekker Inc., New York, 1981) vol. 16.
- [17] C.Kittel, *Introduction to Solid State Physics* (7th Ed.) (John Wiley, New York, 1996).
- [18] R.O. Dillon, I.L. Spain, J.W. McClure, Electronic Energy Band Parameters of Graphite and their Dependence of Pressure, Temperature and Acceptor Concentration. *J.Phys.Chem.Solids.* **38**, 635-645 (1977).